

Integrating Multi-Physics Simulations and Machine Learning to Define the Spatter Mechanism and Process Window in Laser Powder Bed Fusion

Olabode T. Ajenifujah^a, Francis Ogoke^a, Florian Wirth^b, Jack Beuth^a, Amir Barati Farimani^{a,c,d},

^a*Department of Mechanical Engineering, Carnegie Mellon University, Pittsburgh, 15213, PA, USA*

^b*Exentis Group AG, Stetten, 5608, Switzerland*

^c*Department of Chemical Engineering, Carnegie Mellon University, Pittsburgh, 15213, PA, USA*

^d*Machine Learning Department, Carnegie Mellon University, Pittsburgh, 15213, PA, USA*

Abstract

Laser powder bed fusion (LPBF) has shown promise for a wide range of applications due to its ability to fabricate freeform geometries and generate a controlled microstructure. However, components generated by LPBF still possess sub-optimal mechanical properties due to the defects that are created during laser-material interactions. In this work, we investigate the mechanism of spatter formation, using a high-fidelity modelling tool that was built using an open source platform know as OpenFOAM to simulate the multi-physics phenomena in LPBF. The model has the capability to capture the 3D resolution of the melt pool and the spatter behavior. Upon validating the OpenFOAM results with both experimental data and FLOW-3D, a commercial package, we found that the melt pool dimensions (length and width) were closely aligned across various conditions (150 W, 300 W, 450 W) at 1 m/s. The greatest deviation was a 7.8 % decrease in depth at 450 W from OpenFOAM to FLOW-3D, with other deviations falling under 4 %. To understand spatter behavior and formation, we reveal its properties at ejection and evaluate its variation from the melt pool, the source where it is formed. The dataset of the spatter and the melt pool collected consist of 50 % spatter and 50 % melt pool samples, with features that include position components, velocity components, velocity magnitude, temperature, density

and pressure. The relationship between the spatter and the melt pool were evaluated via correlation analysis and machine learning (ML) algorithms for classification tasks. Upon screening different ML algorithms on the dataset, a high accuracy of 95 % and above was observed. Furthermore, the ML model was tested on a different dataset generated using FLOW-3D, a commercial, less computationally expensive tool, but lacks the capability to simulate realistic spatter formation. Our ML model trained on an OpenFOAM dataset was able to classify the region of the melt pool in the FLOW-3D datasets as spatter initiation location. Upon screening 281 FLOW-3D simulation experiments with varying power-velocity combinations, a process map based on spatter volume was established. The process map will serve as a guide towards understanding how the process parameters influence part properties, identifying an AM process window with minimal defects and ultimately enhance repeatability in part production.

Keywords: Additive Manufacturing, Particle Tracking, Process Map, Machine Learning, Defects.

1. Introduction

Additive manufacturing (AM), often referred to as 3D printing, is a transformative approach to industrial production. Laser powder bed fusion (LPBF) is the most common metal AM process. It has several advantages in comparison to conventional manufacturing technologies like milling and casting. LPBF offers design flexibility, quick fabrication of prototypes directly from digital models, reduced material waste, and demonstrates onsite manufacturing capability. The process of using LPBF to create a 3D object starts with spreading a layer of metal particles on the build plate. Then the laser source moving at a certain power and velocity are guided by the laser scanners according to the information in the 3D CAD to melt the regions relating to the design, which then solidifies to form a single layer. The powder spreading, melting and solidifying processes will occur repeatedly until

the final object is formed. LPBF has attracted applications in key economic sectors such as medicine, automotive, aerospace, construction, energy, and prototyping [1, 2]. However, compared to other forms of manufacturing such as machining, casting, and rolling, AM currently has the lowest market share, which is due to poor repeatability, defect formation, and low productivity [1, 3]. Issues with poor repeatability can be attributed to various process parameters such as scanning speed, laser power, beam radius, gas flow path, layer thickness, and hatch spacing involved in operating LPBF. Slight changes in these parameters can propagate, resulting in variability in the properties of parts. Furthermore, the multi-physics phenomena such as heat transfer, solidification, melting, vaporization, and cooling that occur in AM further make it a sensitive process [4–6].

Defects in LPBF could result from the process parameters that generate the melt pool, and the common types are pore [3, 7–12] and crack [13–15]. Taherkhani et al. [16] used the in-situ photoanode sensor to analyze the light signal emitted from the melt pool to quantify the defect and found it to correlate with the process condition. Pores are classified into gas, lack of fusion (LOF) and keyhole induced as a result of their formation from gas entrapment, incomplete melting, or improper print settings, respectively [17]. Rollett et al. [18] used ultrahigh-speed synchrotron X-ray imaging to quantify vapor depressions during melting and identified a clear laser power density threshold for the transition from conduction to keyhole mode. They established quantitative relationships between laser power density, keyhole depth, and front wall angle, providing insight into predicting and controlling keyhole behavior. Spatter ejected from the melt pool is known to cause defects such as surface roughness, porosity, and inclusions [13–15, 19]. Snow et al. [20] demonstrated that spatter particles play a direct role in causing stochastic lack-of-fusion defects in LPBF components. Using spatial statistics, they revealed that the locations of internal flaws are intrinsically connected to the distribution of spatter particles. Toyserkani et al. [21] found that spatter increased surface roughness from $14.4 \mu m$ to $28 \mu m$, recommending avoiding

spatter-rich regions for high-quality parts. The desire to implement multi-lasers to increase printing productivity has been inhibited by spatter generation [22]. Spatter formation results from complex interactions between high-speed vapor, vapor-induced powder movement, and melt pool dynamics. The detrimental effect of spatter could be reduced by manipulating the inert gas flow within the machine. However, reducing the amount of spatter traveling during the LPBF process requires an optimum inert gas flow rate. The high flow rate could lead to spatter generation from the powder bed, such that powder could be lifted by the inert gas, travel around the process chamber and land on a random location based on its trajectory, causing non-uniformity in the arrangement of the powder bed [23]. It is challenging to establish optimum inert gas flow rate for spatter removal, also considering that the relationship will have to be established for varieties of power/velocity combinations which is not only time consuming but also expensive [5, 14, 24, 25]. Providing solution to spatter issues will require a holistic understanding of the physics of laser-material interactions, from melt pool creation to how the material properties can influence the intrinsic nature of the melt pool, leading to the instabilities that cause defect generation across wide process condition space.

The two general approaches to investigating different phenomena in AM are advanced observational technologies and numerical simulation methods. Few experimental studies have been conducted on spatter, Barrett et al. [26] used a high-speed stereovision camera to capture the spatter, then used computer vision to collect their properties for statistical analysis. Previous work by Chen et al. [13] revealed five categories of spatter that can be formed during LPBF: solid, metallic jet, powder agglomeration, entrainment melting spatter, and induced spatter. Additionally, they found that the size, speed, and direction of the spatters vary based on the process condition. Nakamura et al. [27] investigated the behavior of the molten pool during high-power laser welding of titanium alloy using in-situ X-ray monitoring. They highlighted that the upward melt flow around the keyhole surface

contributed to the formation of a liquid column, potentially causing spatter generation. Qu et al. [28] reported that coating Al6061 with TiC nanoparticles effectively eliminated large spatter generation, demonstrating the ability of the nanoparticles to control instabilities during laser-powder bed interactions. This approach resulted in parts with less defects, better consistency, and improved properties. Although advanced monitoring techniques have been used to investigate the mechanism of spatter formation via the physical process, establishing a quantitative relationship between spatter formation and the physical process remains challenging due to experimental limitations in resolution and scale. Determining suitable processing parameters using a trial-and-error approach is time-consuming and expensive. Additionally, it is challenging to fully monitor the complex physical phenomena in the LPBF at microsecond and micrometer scales.

Numerical simulation can offer valuable insight into areas where measurements are challenging or impossible to obtain. It also provides three-dimensional, time-dependent views of keyhole and molten pool behaviors that cannot be directly observed through experiments. Deng et al. [29] developed a model of remote laser spiral spot welding to investigate spatter formation. Their findings revealed that the opening area of the keyhole acts as a primary out-gassing channel, and the instantaneous vapor pressure on the interface is closely related to spatter formation. Many commercial simulation packages such as Ansys, Comsol multiphysics, and StarCCM+ are used for investigating AM. The available AM specific commercial software like FLOW-3D still require adjustments of various numerical parameters, which sometimes are not accessible to the end-users. An open-source software like OpenFOAM (Open Field Operation and Manipulation), is flexible in implementing additional features to address novel problems and processes occurring during AM process [30, 31]. However, modeling AM process by taking into account the multiphysics involved in the melt pool dynamics and spatter generation is computationally expensive.

The high computational cost associated with high-fidelity simulations has motivated

their synergy with ML tools, especially where a large scale of simulation experiments is necessary, such as in understanding defect formation processes, part design optimization, and the discovery of metamaterials and process monitoring [2, 32–42]. Hemmasian et al. [43] utilized FLOW-3D simulation software to generate data sets for LPBF processes and trained a convolutional neural network to predict the temperature field using only the process conditions as input to the model. DebRoy et al. [44] integrated physics-informed machine learning, mechanistic modeling, and experimental data to identify key variables that shed light on the physics behind defect formation in AM. Using balling defects in LPBF as an example, they utilized peer-reviewed experimental data from the literature. This approach makes it possible to extend AM modeling and simulation to a larger scale and encompass a wider range of parameters. Ren et al. [11] employed X-rays to monitor pore formation in LPBF while simultaneously using a thermal imaging system for observations. This setup enabled the authors to develop a highly accurate method for detecting pore formation from thermal signatures, utilizing a machine learning approach.

The potential for synergy of ML with physics-based simulation to understand spatter formation remains unexploited, which could have been due to limited studies and understanding of spatter as compared to other forms of defects. Spatter generation is influenced by complex and often non-linear interactions between multiple process variables. ML models are adept at capturing these complex relationships in high-dimensional data [35, 41]. ML can provide predictive insights that are not easily discernible through traditional physics-based modeling. Lastly, ML can help optimize process parameters not only to avoid spatter but also to achieve the best possible results in terms of speed, cost, and material properties [15]. Using ML models, a deeper understanding of the spatter can be achieved, leading to improved control, improved process efficiency, and superior material characteristics in manufacturing and other material processing fields.

In this study, we develop a high fidelity multi-physics model based on OpenFOAM sim-

ulation to study the spatter ejection in LPBF. Hot spatter is known to cause detrimental effects on the build component, act as a source of porosity, and roughness as it can create local melting upon landing on the solid part as it is known to originate from the melt pool. Compared to powder spatter, the formation of hot spatter and its role in inducing macroscopic defects have a more significant impact on the quality of the LPBF process [45]. Therefore, our work aims at developing a methodology specifically for analyzing the properties that differ between the ejected fluid and the melt pool, as detecting fluctuations in the melt pool is critical for ensuring satisfactory quality control during part fabrication. Having established these studies on the behavior of hot spatter ejection, not only will misclassification of the different types of spatter be prevented, their effect will be captured and deconvoluted in the future investigation. We develop a tracking algorithm specifically for the LPBF dataset generated with OpenFOAM, which differentiates between spatter and the melt pool, links data across consecutive time steps, and extracting properties at each time step, such as temperature, velocity, location, and density in 3D. We unveil the relationship between the spatter ejection and the melt pool via statistical analysis, whereby spatter is detected at a short time scale ($5 \mu\text{s}$), paving the way to quantifying the fluctuation in the melt pool for good quality control. Upon coupling our ML model with multiphysics models, for the first time we reveal importance of different parameters to the spatter ejection and formulate a spatter formation mechanism. In addition to using ML models for classification tasks and to establish trends in the feature importance, we complement it with an explainable AI technique which provide insights into the range of the feature values that positively contribute spatter predictions. Furthermore, our ML model was applied and tested against datasets generated from FLOW-3D, a prevalent yet computationally economical software extensively employed in AM. However, FLOW-3D implements restrictive assumptions that limit spatter simulation to improve computational cost. Specifically, the gas dynamics within the keyhole are not directly simulated, and are instead approximated by estimates of the re-

coil pressure and mass transfer. Additionally, FLOW-3D lacks the tangential surface tension component [46, 47]. In contrast, our OpenFOAM model keyhole gas dynamics and implements tangential surface tension following the method by Wirth et al. [1]. By leveraging the respective strengths of OpenFOAM and FLOW-3D simulations, augmented with machine learning (ML), a reduced-order methodology was developed to accelerate spatter process map generation in LPBF. This approach facilitates rapid and accessible quantification of generated spatter relative to the expected volume. This enables the creation of a comprehensive process map, providing insight into the spatter formation mechanism in additive manufacturing. This map can be used as a visualization tool to identify optimal process windows and parameters, enabling the printing of parts with low porosity and high-quality surface finish.

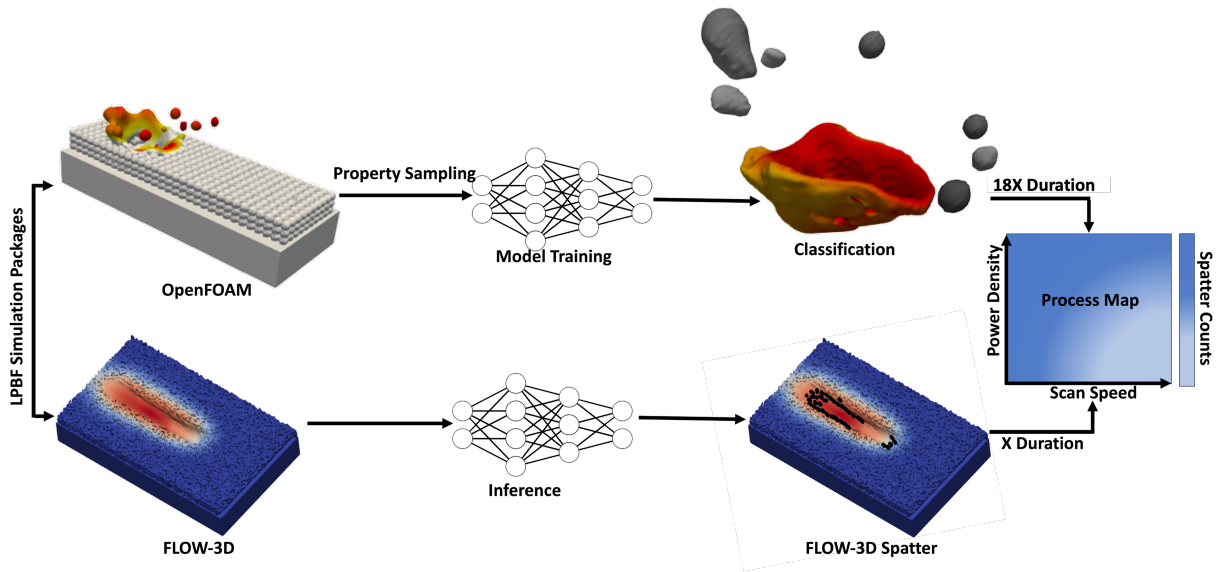


Figure 1: Spatter ejection and melt pool parameters from OpenFOAM simulations were used as input for machine learning classification tasks. The trained models were tested on FLOW-3D datasets, a commercial software that lacks realistic spatter simulation capability to generate a process map. A $5 \mu m$ LPBF simulation in FLOW-3D and OpenFOAM requires 4 hours and 72 hours respectively on the same machine.

2. Methods

2.1. Simulation of LPBF via OpenFOAM

A CFD model was developed using OpenFOAMv2012 to analyze the complex physical phenomena that occur during the LPBF process. A newly introduced icoReactingMultiphaseInterFoam (IRMIF) solver [1, 30, 48] was used. The IRMIF solver is based on the volume-of-fluid (VOF) method, where each phase is immiscible, and a clear boundary between each phase is calculated. The IRMIF solver handles fluid mechanics, including turbulent flow, laser beam sources with arbitrary beam shapes, heat transfer, and phase transitions such as solidification, melting, and evaporation. However, the solver did not account for the Marangoni effect due to the absence of the tangential component of the surface tension. The presence of the tangential component could influence the shape of the melt pool, leading to denudation, spatter, and pore formations. The tangential component of the surface tension is added to the solver following the modification by Wirth et al. [22] to incorporate the Brackbill equation [49] which enables the implementation of surface tension forces in the VOF method as shown in equation (1)

$$F_s = [\sigma\kappa\vec{n} + (\nabla\sigma - \vec{n}(\vec{n} \cdot \nabla\sigma))] \cdot \frac{2 \cdot \rho(x)}{\rho_1 + \rho_2} \cdot \frac{|\nabla\rho(x)|}{\rho_2 - \rho_1} \quad (1)$$

The parameters in Equation (1) include the surface tension σ , the interface curvature κ , the normal vector of the interface \vec{n} , and the densities ρ_1 and ρ_2 of the two phases at the interface. In brackets of Equation (1), the first term corresponds to the normal component of the surface tension force, while the second term corresponds to the tangential component. The factor $\frac{2 \cdot \rho(x)}{\rho_1 + \rho_2}$ acts as a weight function that redistributes the surface tension force smeared to the denser phase. The term $\frac{|\nabla\rho(x)|}{\rho_2 - \rho_1}$ determines the position of the interface where it is non-zero.

Using the VOF method, the dynamic geometry of the free surface (gas/ metal interface)

was captured. The volume fraction satisfies equation (2). In OpenFOAM, an additional convective term is introduced to the VOF, adapting it to a two-fluid Eulerian system [50], which depends on the compression velocity \vec{n} . This velocity is active only in the interface cells due to the term $\alpha_1(1 - \alpha_1)$. This artificial velocity helps compress the interface by reducing the numerical diffusion of the volume fraction α_1 while preserving its boundedness [51]. Since only the VOF is solved by the solver used in this study, the forces at play drive the fluid flow, with the velocity determined through the momentum balance to account for ejection from the melt pool. Since the force acting on the particles is intrinsic to the fluid flow, as it is a viscous fluid rather than individual particles, solving the velocity field captures the dynamics of spatter ejection.

$$\frac{\partial \alpha_1}{\partial t} = -\vec{\nabla} \cdot (\alpha_1 \vec{u}) - \vec{\nabla} \cdot \vec{u} \alpha_1 (1 - \alpha_1) \quad (2)$$

In the situation of the mixture of vapor and nitrogen, the model applies a weighting average based on the composition of each component in the mixture in equation (3-7) to the value of its physical properties, such as density ρ , viscosity μ , thermal conductivity k and specific heat capacity C as listed in Table 1.

$$\alpha_1 + \alpha_2 = 1 \quad (3)$$

$$\rho = \alpha_1 \rho_1 + \alpha_2 \rho_2 \quad (4)$$

$$\mu = \alpha_1 \mu_1 + \alpha_2 \mu_2 \quad (5)$$

$$k = \alpha_1 k_1 + \alpha_2 k_2 \quad (6)$$

$$C = \alpha_1 \frac{\rho_1}{\rho} C_1 + \alpha_2 \frac{\rho_2}{\rho} C_2 \quad (7)$$

The value of either α_1 or α_2 ranges from 0 to 1, where α_1 and α_2 are the volume fractions of

the phase of the element, \vec{u} is the flow velocity, t is the time. The finite volume method was used to compute the fluid flow, based on continuity and transient Navier-Stokes equation, as described in equations (8) and (9) respectively.

$$\frac{\partial \rho}{\partial t} + \nabla \cdot (\rho \vec{u}) = 0 \quad (8)$$

$$\frac{\partial(\rho \vec{u})}{\partial t} + \nabla \cdot (\rho \vec{u} \otimes \vec{u}) = \nabla \cdot \left\{ -p \cdot \vec{I} + \mu [\nabla \vec{u} + (\nabla \vec{u})^T] \right\} + \vec{F} \quad (9)$$

where ρ is the density, \vec{u} is the fluid flow velocity vector, t is the time, p is the pressure, I is the identity tensor, μ is the dynamic viscosity and \vec{F} is the volume force vector. Rapid heating to high temperatures causes the molten material to evaporate, generating a recoil pressure within the melt pool. This recoil pressure, produced by the vapor jet, drives the melt surface downward, creating a vapor depression. The recoil pressure is modeled using the Clausius–Clapeyron equation to calculate the saturated vapor pressure, adjusted by a coefficient that accounts for the backward flux of the evaporated material, as shown in equation 10 [52–54].

$$\vec{P}_r = 0.54 P_0 \exp \left[\frac{L_v M (T - T_v)}{R T T_v} \right] \vec{n} |\nabla \alpha_1| \frac{2\rho}{\rho_{\text{metal}} + \rho_{\text{gas}}} \quad (10)$$

where P_0 is the ambient pressure, L_v is the latent heat of evaporation, T_v is the evaporation temperature, M is the molar mass, and R is the universal gas constant. The energy equation in equation (11) was used to compute the temperature field.

$$\rho \frac{\partial E}{\partial t} = -\rho \vec{\nabla} \cdot \vec{u} E + \vec{\nabla} \cdot (k \vec{\nabla} T + \vec{\tau} \cdot \vec{u}) + q_v + q_{\text{rad}} + q_{\text{laser}} \quad (11)$$

where E is the mixed energy, k is the thermal conductivity, T is the temperature, $\vec{\tau}$ is the stress tensor. q_v is the heat loss due to vaporization (Equation 12), q_{rad} is the heat loss due

to radiation (Equation 13), q_{laser} is the heat input from the laser beam (equation 14).

$$q_v = -0.82 \frac{l_v M}{\sqrt{2\pi MRT}} P_0 \exp \left[\frac{l_v M (T - T_v)}{RTT_v} \right] |\nabla \alpha_1| \frac{2\rho C_p}{\rho_{\text{metal}} \rho C_{\text{pmetal}} + \rho_{\text{gas}} C_{\text{pgas}}} \quad (12)$$

$$q_{\text{rad}} = -\sigma_s \varepsilon (T^4 - T_{\text{ref}}^4) |\nabla \alpha_1| \frac{2\rho C_p}{\rho_{\text{metal}} \rho C_{\text{pmetal}} + \rho_{\text{gas}} C_{\text{pgas}}} \quad (13)$$

Where C_p is the specific heat capacity, L_m is the latent heat of melting, σ_s , ε , T_{ref} are the Stefan-Boltzmann constant, emissivity and ambient temperature respectively. The IRMIF solver uses the discrete transfer radiation model, which takes the laser beam into account, passing through VOF phases [55]. The laser energy was applied in the form of a body heat source and goes into the depth of the material. A Gaussian intensity distribution ($D_{4\sigma} = 100 \mu\text{m}$) is applied to the laser beam.

$$q_{\text{laser}} = \frac{f_{\text{absorb}} I}{\Delta y} \quad \text{where } I = \frac{2\xi P}{\Pi r^2} \exp \left[\frac{-2(x + v_0 t - x_0)^2 + (z - z_0)^2}{r^2} \right] \quad (14)$$

Where I is the beam power density, f_{absorb} is the percentage of laser energy occupied by the element, P is the laser power, ξ is the absorption coefficient, r is the beam radius, (x_0, z_0) describes the starting position of the laser beam, v_0 denotes the scanning velocity and Δy represents the size of the numerical grid. IRMIF uses the Lee mass transfer model in equation (15) to calculate the solidification (or also melting) process, better described in [56] and the original formulation of Lee [57].

$$m = C' \rho \alpha \frac{T - T_A}{T_A} L \quad (15)$$

In equation 15, m is the mass transfer between phases, C' is Lee's model constant, α is the phase volume fraction, T is the current temperature, T_A is the solidification or melting temperature, L is the latent heat. It should be noted that the same set of equations works

for both solidification ($T < T_A$ and C' negative) and melting ($T > T_A$ and C' positive) [58].

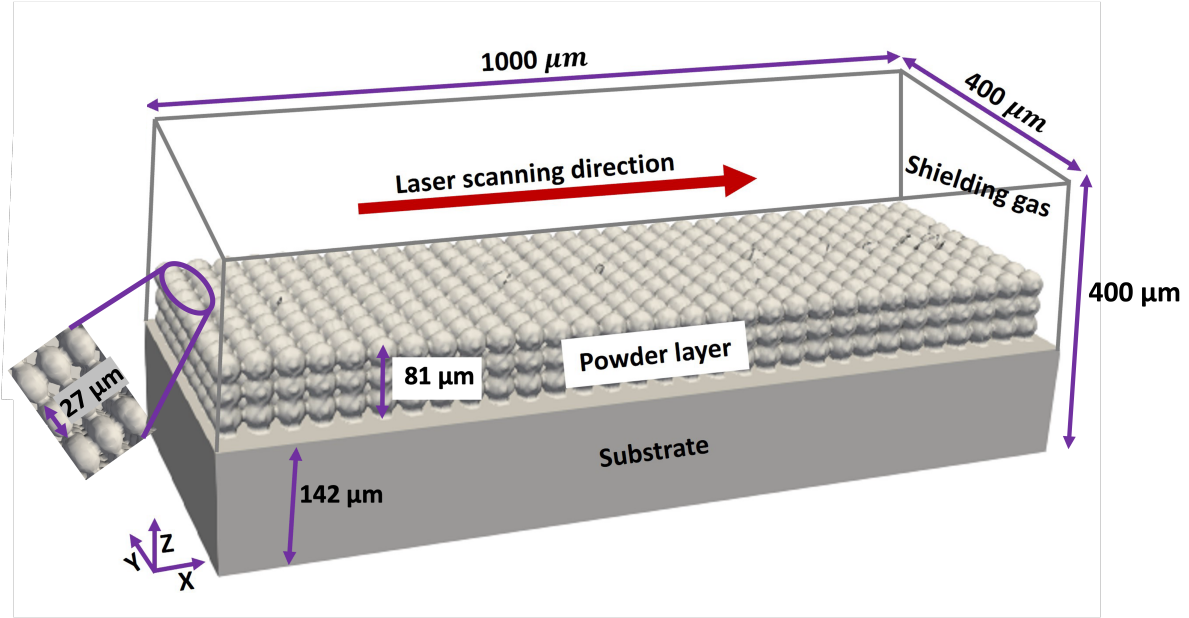


Figure 2: Schematic illustration of the computational domain with random packing of stainless steel powder bed in for OpenFOAM simulation.

The dimension of the simulation domain is $1000 \mu m \times 400 \mu m \times 400 \mu m$ as shown in Figure 2. A previous study by Liu et al. [59] indicated that to minimize or eliminate flowability uncertainty, it is preferable to reduce the powder size distribution to achieve near homogeneity. They found that the narrower the particle size distribution, the higher the mechanical resistance and hardness of the printed components. Another work by Young et al. [60] generated six sets of powder distribution that vary from 0 - 100 % of 15–25 μm powder in a mixture with 35–48 μm powder. They observed a general downward trend for spatter volume as the percentage of 15–25 μm powder increased. Therefore, we choose to assume a uniform distribution of powder sizes for LPBF performance optimization. Powders of sizes 27 μm , a layer thickness of 81 μm , and a bare plate height of 142 μm were used. Adaptive mesh was implemented in OpenFOAM where the mesh size along the x-axis and

the y-axis is fixed at $2.5 \mu\text{m}$ and $5 \mu\text{m}$, respectively, while the z-axis varies from $2.5 \mu\text{m}$ to $8.74 \mu\text{m}$ to generate the total number of 2688000 cells.

Table 1: Material parameters implemented for the simulation of the SS316L melting process in OpenFOAM simulation [54, 61], while the subscript s represents the solid phase, l for the liquid phase, v for the vapor and n for the shielding gas nitrogen

Parameter	Value	Units
Density, ρ , 298 K	7618	kg/m ³
Density, ρ , 1923 K	6468	kg/m ³
Specific heat solid, $C_{p,s}$,	592.7	J/kg/K
Specific heat liquid, $C_{p,l}$, 1923 K	1873	J/kg/K
Specific heat vapor, $C_{p,v}$	775	J/kg/K
Specific heat nitrogen, $C_{p,n}$	1035	J/kg/K
Thermal conductivity solid, k_s , 298 K	24.57	W/m/K
Heat of fusion, Hf_l	2.7×10^5	J/kg
Heat of evaporation, Hf_v	449	J/kg
Dynamic viscosity liquid, μ_l	3.16×10^3	J kg/m/s
Dynamic viscosity vapor, μ_v	1.79×10^6	J kg/m/s
Prandtl number liquid, Pr_l	0.1214	J kg/m/s
Prandtl number vapor, Pr_v	0.7	J kg/m/s
Prandtl number nitrogen, Pr_n	0.7721	J kg/m/s
Surface Tension, σ	1.882	kg/s ²
Liquidus Temperature, T_L	1723	K
Solidus Temperature, T_S	1658	K
Absorptivity	0.55	
Latent Heat of Fusion, ΔH_f	2.6×10^5	J/kg
Latent Heat of Vaporization, ΔH_v	7.45×10^6	J/kg

2.2. FLOW-3D Simulation

FLOW-3D (v11.2) simulations are performed to accelerate the development of the process map (Figure 1). FLOW-3D is a multiphysics simulation software produced by Flow Science, which provides more rapid estimations of the melt pool behavior than OpenFOAM. This reduction in computational expense is achieved in part by abstracting the vapor phase dynamics to estimates of the applied pressure and mass transfer at the surface of the melt pool. To create a FLOW-3D simulation data set, 283 SS316L single-track bare plate experiments are performed at varying processing parameters for a total length of $600 \mu\text{s}$.

During simulation, the FLOW-3D package solves the equations that describe the mass transfer, momentum transfer, and energy transfer during the melting process.

This simulation is carried out on a structured Cartesian mesh, with mesh elements sized at $10 \mu\text{m}$. More specific information on the equations solved and the physical phenomena considered during the simulation can be found in [32, 43, 46, 47, 62].

2.3. Spatter Extraction and Analysis

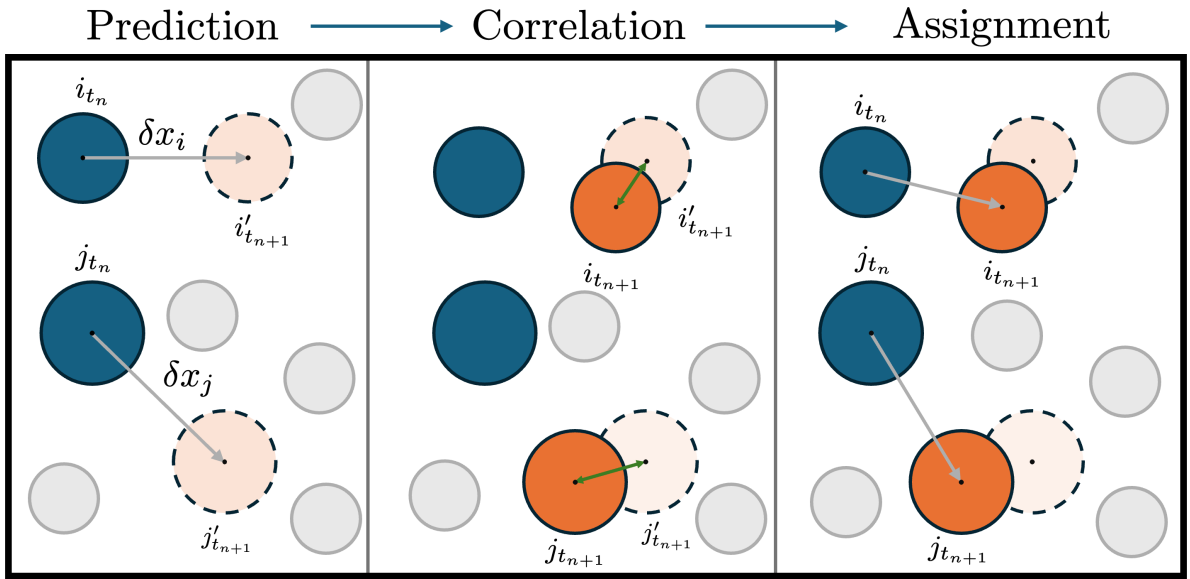


Figure 3: A tracking algorithm is implemented to consistently identify spatter particles as they move through the domain. The tracking process is demonstrated for two sample particles i and j , between the timesteps n and $n + 1$. During the tracking process, the velocity field of the particle is used to predict an estimated displacement δx_i within $t_{n+1} - t_n = \Delta t$. Next, the actual particle positions at the next timestep, $i_{t_{n+1}}$, are correlated to the estimated displacement values $i'_{t_{n+1}}$ based on a nearest neighbors assignment. Following this, each particle i_{t_n} is linked to $i_{t_{n+1}}$, completing the tracking process.

The OpenFOAM simulation data are processed to extract properties of both the ejected spatter and the melt pool. The cell-level simulation information is extracted for processing in Python, where each field is represented as a three-dimensional matrix defined by the mesh. As part of this information, three fields – α_g , α_s and α_l denote the volume fraction of the gas phase, the solid phase, and the liquid phase, respectively. To differentiate the powder bed,

spatter, and melt pool from the gaseous phases of the simulation, the gas volume fraction α_g is truncated at 0.5, masking cells in the domain occupied by inert gas or metal vapor from the current analysis.

In this scenario, the ejected fluid spatter droplets are treated as particles in our studies to denote a connected set of fluid cells that are disconnected from the larger melt pool. Connected component analysis [63] is used to isolate individual spatter particles for further analysis. To do so, a binary field is constructed from α_g by applying a threshold at 0.5, assigning 1 to solid cells and liquid cells and 0 to gas phase cells. The spatter particles, powder bed and melt pool are then identified by applying the Union-Find algorithm to the binary array, which assigns unique labels to each disconnected object within the 3D domain [64, 65]. The largest contiguous object is identified as the composite melt pool and powder bed structure, and all other objects above a size-based noise threshold are considered to be spatter particles. Specifically, this threshold acts as a lower bound on the size of the particles, where particles comprised of less than eight connected cells are removed from the analysis. Following this processing step, the mesh elements that construct each particle can be used to extract particle-level field information.

To extract the kinematics of the particle behavior, the positions of the particles must be tracked across the evolution of the simulation. During the connected components analysis, individual particles are identified without any intrinsic order. Therefore, an additional processing step is required to identify the mapping between particles at subsequent timesteps. We perform this tracking operation as a three-stage process – prediction, correlation and assignment. Given a set of m particles at timestep t_n and a set of k particles at timestep t_{n+1} , the goal of this process is to associate each of the m particles at t_n with either the index of the corresponding particle at t_{n+1} , or a condition indicating that the particle trajectory has ended. The remaining particles at timestep t_{n+1} that have not been associated with a particle at timestep t_n are considered to have formed at timestep t_{n+1} (Figure 3).

During the first phase of the tracking process, the velocity of each particle is used to estimate the displacement that occurs over a time Δt . Specifically, the average of the velocity fields for the cells comprising each particle is used to estimate the displacement $\delta \mathbf{x}_i$ (Equation 16), assuming a constant velocity over the timestep Δt . In Equation 16, N_s refers to the number of cells comprising a particle, and \mathbf{v}_s refers to the velocity of each individual cell.

$$\delta \mathbf{x}_i = \frac{\Delta t}{N_s} \sum_{s=1}^{N_s} \mathbf{v}_s \quad (16)$$

This displacement defines an estimate of the position of each particle at time t_n at the next timestep,

$$\mathbf{x}_{i'}|_{t_{n+1}} = \mathbf{x}_i|_{t_n} + \delta \mathbf{x}_i \quad (17)$$

For each of these estimates $\mathbf{x}_{i'}$, we find the nearest neighbor to the estimate within the set of k particles at timestep t_{n+1} . If this nearest neighbor lies within a specified maximum distance Δx , the nearest neighbor is assigned to have the same index i . However, if no such neighbor is found, the trajectory is assumed to have ended with the particle either leaving the domain or impacting the powder bed. To improve the computational efficiency of the tracking process, a $k - d$ tree structure is queried to identify the pairwise distances between the sets of particles considered. With the tracking process complete, the kinematic properties of each particle, such as the magnitude and direction of motion, can be computed.

To sample points from the melt pool surface, the volume fractions of the gas and liquid phases are used to define the melt pool morphology. Specifically, α_g is first used to threshold and identify the partially molten powder bed. From the points comprising the partially molten powder bed, the melt pool is identified by isolating values with a liquid volume fraction α_l greater than 0.5. The surface is then identified by finding the grid cells with the highest value of α_g within the points comprising the melt pool. During the sampling process,

we extract the average of a specific field within a $n_r \times n_r \times n_r$ bounding cube centered at a specific point along the surface, only taking into account the points within the bounding cube that lie within the melt pool, where n_r is an arbitrarily selected parameter describing the size of the region investigated. We sample n_i points from the melt pool at each timestep, where n_i is the number of spatter particles ejected at time i . Each sample contains the mean of the position, velocity, density and temperature of the sampled region. Once this data has been sampled, the properties of the sampled regions are compared to the properties of the spatter particles.

2.4. Machine Learning Methodology

2.4.1. Data Collection and Hyper-Parameter Optimization

Our dataset was extracted from OpenFOAM simulation of two experiments, one conducted at a laser power of 545 W with a scan speed of 2 m/s, and another conducted at a laser power of 690 W and scan speed of 2 m/s. The spatter and the melt pool features were extracted using ParaView. The extracted features were used to validate our developed tracking algorithm, which is efficient in extracting not only spatter and melt pool properties but also the capability to track spatter trajectory. Detecting variations in the property distributions between the ejected spatter and the melt pool can enhance classification tasks. We implement different ML models as discussed in the Appendix A. to establish the performance trends for the spatter/melt pool classification task. From OpenFOAM experiments, we collected 488 data points, evenly split between the two classes (50 % spatter and 50 % melt pool). For the ML tasks, the dataset was divided into training (70 %) and testing (30 %) subsets using train test split, with a fixed random seed to ensure reproducibility of the results. Hyperparameter optimization was performed using GridSearchCV with 5-fold cross-validation, using the ROC-AUC score as the evaluation metric. The grid search explored a predefined hyperparameter space as listed on Table 2, the best parameters were identified by selecting the combination that maximized the average ROC-AUC score across

the cross-validation folds. These parameters were then used to train the model in the training dataset. Predictions and probabilities were generated for both the training and testing sets. Model performance was evaluated using metrics including accuracy, F1-score, balanced accuracy, and ROC-AUC to assess the model’s predictive performance and generalization ability.

2.4.2. SHapley Additive exPlanations as an Explainable AI

SHapley Additive exPlanations (SHAP) implement a game-theoretic approach to describe how the ML models make predictions. It is based on the concept of Shapley values from cooperative game theory, where contributions of individual players (features) to the overall game outcome (model prediction) are calculated fairly [66]. SHAP values assign each feature a contribution value for every prediction, ensuring both global and local interpretability. The method guarantees local accuracy (the sum of SHAP values equals the model prediction) and consistency (a feature with increased contribution in a newer model will not have a lower SHAP value).

Mathematically, the SHAP value for a feature i is given by:

$$\phi_i = \sum_{S \subseteq N \setminus \{i\}} \frac{|S|!(|N| - |S| - 1)!}{|N|!} [f(S \cup \{i\}) - f(S)], \quad (18)$$

where S is a subset of features, N is the set of all features, and $f(S)$ represents the model prediction with features in S . This ensures that SHAP fairly distributes the prediction among features by evaluating all possible subsets.

SHAP provides two key benefits: (1) Global interpretability, where aggregated SHAP values reveal feature importance across the dataset, and (2) Local interpretability, where SHAP values explain individual predictions by quantifying each feature’s contribution.

Partial Dependence Plots (PDPs) provide a visual representation of how one or two features influence model predictions, independent of other features. For a single feature X_j ,

Table 2: Grid search hyperparameters range and the best value used for ML models.

Model	Grid Search Parameters	Used/Best Parameters
RF	{ 'n_estimators': range(1, 100), 'max_depth': range(3, 12), 'max_features': ['sqrt'] }	{ 'criterion': 'entropy', 'max_depth': 11, 'max_features': 'sqrt', 'n_estimators': 90 }
GB	{ 'n_estimators': range(50, 200, 50), 'learning_rate': [0.01, 0.1, 0.2], 'max_depth': range(3, 6), 'min_samples_split': [2, 5, 10], 'min_samples_leaf': [1, 3, 5] }	{ 'learning_rate': 0.2, 'max_depth': 4, 'min_samples_leaf': 5, 'min_samples_split': 2, 'n_estimators': 150 }
Bagging	—	BaggingClassifier(base_estimator=extra_tree, n_estimators=10, max_samples=0.8, max_features=0.8, bootstrap=True, random_state=42, n_jobs=-1)
ExtraTrees	{ 'n_estimators': range(10, 100, 10), 'max_depth': range(3, 10), 'max_features': ['sqrt', 'log2', None], 'criterion': ['gini', 'entropy'] }	{ 'criterion': 'entropy', 'max_depth': 9, 'max_features': None, 'n_estimators': 90 }
LGBM	{ 'n_estimators': [100, 200], 'learning_rate': [0.01, 0.1, 0.2], 'max_depth': [-1, 10, 20], 'num_leaves': [31, 50], 'min_child_samples': [10, 20], 'subsample': [0.8, 1.0], 'colsample_bytree': [0.8, 1.0] }	{ 'colsample_bytree': 1.0, 'learning_rate': 0.2, 'max_depth': -1, 'min_child_samples': 20, 'n_estimators': 200, 'num_leaves': 31, 'subsample': 0.8 }
KNN	{ 'n_neighbors': range(1, 100), 'weights': ['uniform', 'distance'], 'p': [1, 2] }	{ 'n_neighbors': 16, 'p': 1, 'weights': 'distance' }
SVC	{ 'svc_C': [0.1, 1, 10, 100], 'svc_kernel': ['linear', 'rbf', 'poly'], 'svc_gamma': ['scale', 'auto'], 'svc_degree': [2, 3] }	{ 'svc_C': 10, 'svc_degree': 2, 'svc_gamma': 'scale', 'svc_kernel': 'rbf' }

the partial dependence function is defined as [67]:

$$\text{PDP}(X_j) = \frac{1}{n} \sum_{i=1}^n f(X_{i,-j}, X_j) \quad (19)$$

where $X_{i,-j}$ denotes all features except X_j . Single-feature PDPs illustrate the marginal effect of a feature, while pairwise PDPs show the joint effect of two features on predictions. PDPs are particularly useful for validating model interpretability and identifying nonlinear relationships.

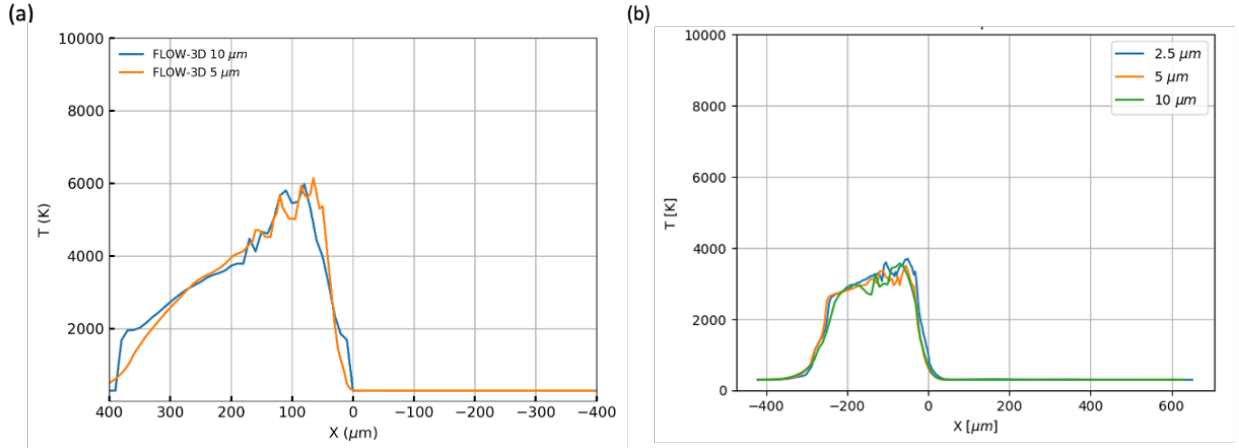


Figure 4: Mesh dependence studies on the temperature profile (a) FLOW-3D (b) OpenFOAM

3. Results and Discussion

3.1. Validation of Numerical Simulations

Mesh independence experiments were carried out on OpenFOAM and FLOW-3D as shown on Figure 4. Mesh sizes of $5 \mu m$ and $10 \mu m$ were compared in FLOW-3D, while mesh sizes of $2.5 \times 5 \times 2.5$ - $8.74 \mu m$, $5 \mu m$ and $10 \mu m$ were compared in OpenFOAM. Close matches were observed in OpenFOAM and FLOW-3D, indicating that the mesh resolves heat transfer at the chosen resolution across the mesh sizes investigated.

The simulation parameters and physics in the FLOW-3D and OpenFOAM models have been calibrated to match the experimental thermal results, following the methodology proposed by Myers and Quirarte et al. [62]. In these experiments, SS316L single-bead tracks were printed without powder using a TRUMPF TruPrint 3000 L-PBF machine. High-speed

imaging of the melt pool was achieved using a Photron FASTCAM mini-AX200 color camera, capturing images at a rate of 22,500 frames per second, where each pixel corresponds to an area of $5.6 \mu m$. These images were subsequently converted into pixel-by-pixel temperature data using the two-color method, which helps to reduce the impact of emissivity's temperature dependence by using the intensity ratios from the camera's red and green channels. Myers and Quirarte et al. [62] provide detailed experimental methodologies and results. The dimensions of the melt pool are determined by sectioning, etching, and measuring the dimensions of the single-bead tracks.

These comparisons are conducted at the laser powers that are within the range at which our OpenFOAM simulations for these studies were carried out (150 W, 300 W, and 450 W), with the scanning speed maintained at 1 m/s as shown in Table 1. At 100 W and 450 W while the scanning speed is 1 m/s, the width and depth of OpenFOAM simulation and experiment results are within the same range, while at 350 W and scanning speed of 1 m/s, there were slight variations. On comparing OpenFOAM melt pool dimensions to the lower bound of the width and depth of the experimental measurements at 300 W and 1 m/s, deviations of 7.8 % and 1.3 % respectively were observed. These results show close agreements between experimental studies and OpenFOAM with respect to the measured depth and width. The deviation may be due to the experimental settings of the laser orientation as it was positioned at an angle of approximately 20° during the interaction with the build plate for the accommodation of the imaging apparatus [62]. Ultimately, developing a process window using the Flow3D dataset via the ML model trained on the OpenFOAM dataset requires measurement agreements between both simulations. Slight variations with respect to the width and depth are observed with the highest being the measured depth at 450 W with 7.8 % decrease from OpenFOAM to Flow3D simulations. Further validation via comparison between the FLOW-3D, OpenFOAM data and experimental temperature profiles is displayed in Figure 3 for the set of process conditions, where the experimental

Table 3: The melt pool dimensions comparison of experiment, FLOW-3D and OpenFOAM at a fixed speed of 1 m/s. The experimental widths and depths provided are generated from the solidified melt track, while the reported errors are in two standard deviations.

Power [W]	150	300	450
Experimental width (μm)	105 ± 7.98	161 ± 9.00	181 ± 4.62
Flow3D width (μm)	95	138	180
OpenFOAM width (μm)	100	140	176
Experimental depth (μm)	31.0 ± 3.32	78.9 ± 4.86	155 ± 8.58
Flow3D depth (μm)	35	80	140
OpenFOAM depth (μm)	38	73	152

measurements combine images captured at different camera exposure times (1.05 μs , 1.99 μs , 6.67 μs , and 20 μs). Experimental temperature values below 2000 °C are not visible via high-speed imaging could be due to the low intensity of the green and red thermal radiation at low temperatures. The deviation in the experimental measurements is due to the plume emission and transmission above the melt pool that interferes with temperature measurement and obscure the front and side melt pool boundaries with temperature. However, a close range and similar rise-and-fall profile can be observed between the experimental and simulation results, particularly for the larger section where the experimental melt pool dataset was collected [62]. In addition to validating the melt pool dimensions and the temperature distribution, the dynamics of the spatter simulated in OpenFOAM were validated using the experimentally reported velocities by Ly et al [19]. The velocity distribution from OpenFOAM was extracted (Figure 6a) and compared to the values reported by Ly et al. on the y-axis of Figure 6b, which ranged from 2.5 m/s to 20 m/s for recoil pressure spatter and hot spatter as shown Figure 6b, demonstrating agreement with the OpenFOAM velocity distribution.

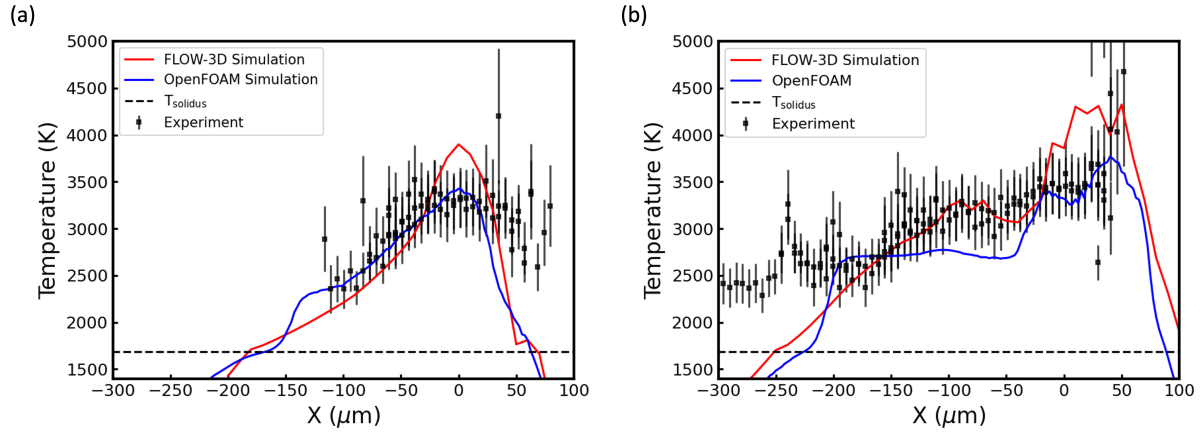


Figure 5: Implementation of the two-color thermal imaging method as described in [62] for the comparison of the observed surface temperatures for SS316L with the corresponding surface temperatures obtained from modelling packages: a) Measurements taken at $P = 150$ W, $V = 1000$ mm/s b) Measurements taken at $P = 300$ W, $V = 1000$ mm/s. The error bars from the experimental measurements represent combined uncertainties in emissivity and signal, as detailed in [62].

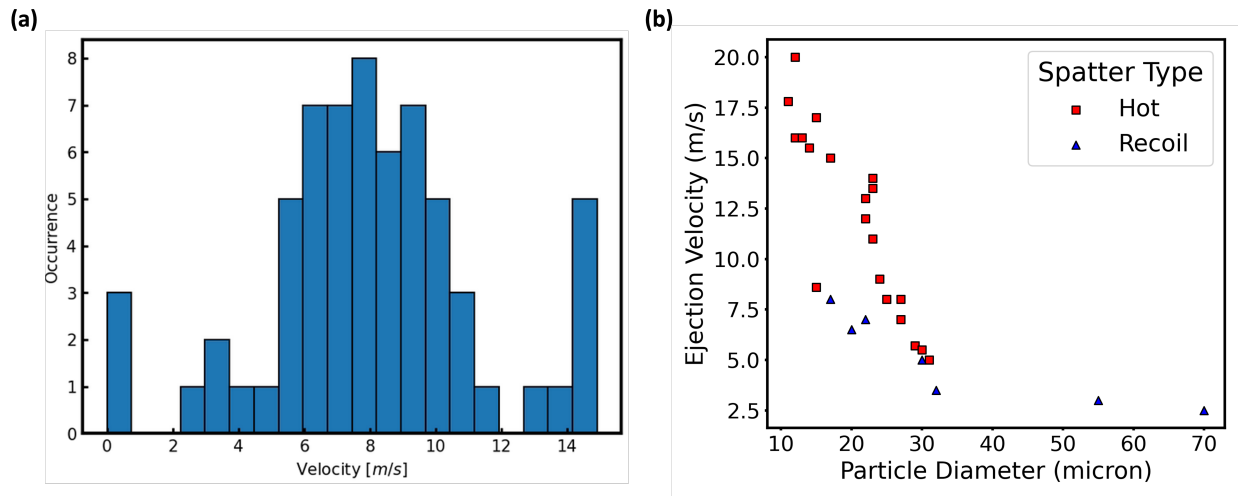


Figure 6: Spatter dynamic validation via the magnitude of the velocity (a) OpenFOAM velocity distribution (b) Reported velocity by Ly et al. [19].

3.2. Spatter and Melt Pool Property Correlations

The behavior of the melt pool depends on the process parameters, and while the ejected spatter originates from the melt pool, likely its properties are different. However, the exact nature and extent of these differences remain unknown as a result of the lack of equipment

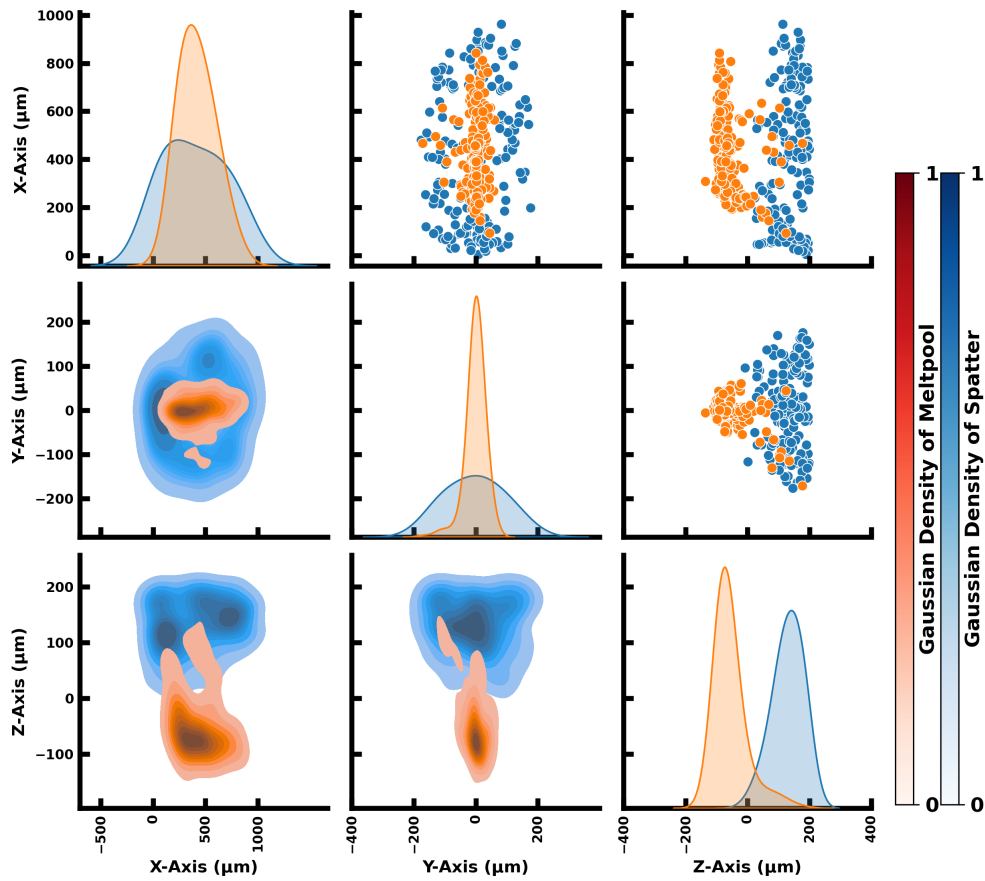


Figure 7: Pairplot correlating spatial distribution of the melt pool and the spatter ejection through the histogram along the diagonal, Kernel Density Estimation (KDE) plots to the left of the diagonal and scatter plot to the right of the diagonal .

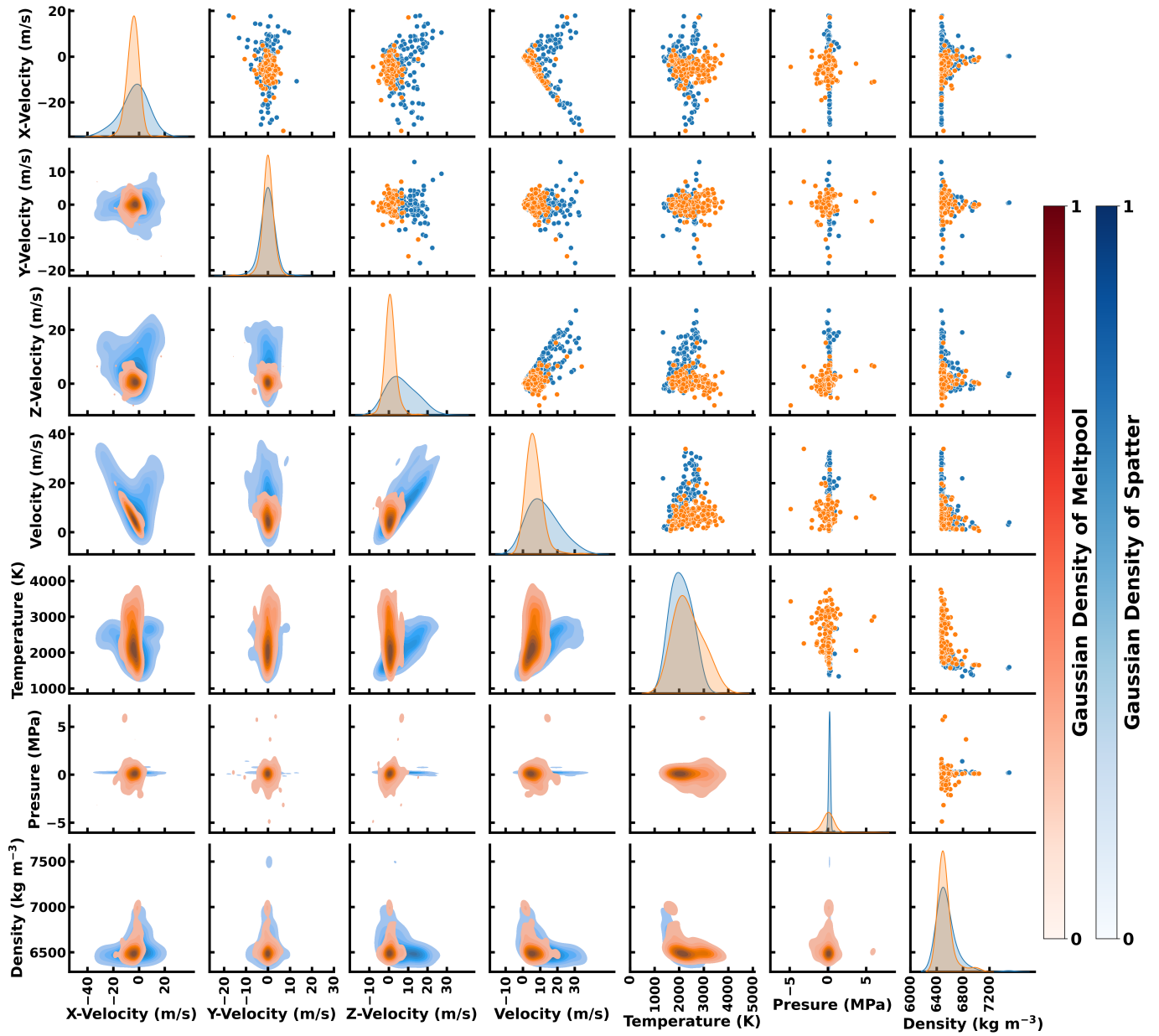


Figure 8: Pairplot correlating different measured properties of the melt pool and the spatter ejection through the histogram along the diagonal, Kernel Density Estimation (KDE) plots to the left of the diagonal and scatter plot to the right of the diagonal.

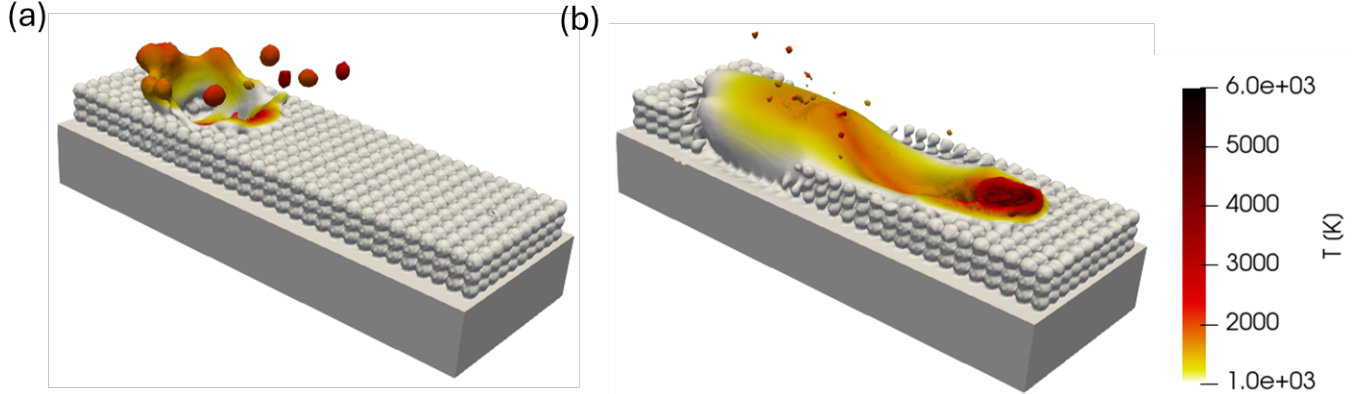


Figure 9: OpenFOAM simulation at 509 W and 1.5 m/s displaying spatter event at different timestep (a) spatter event 110 μs (b) Spatter event at 440 μs .

with the precision and sensitivity to detect such subtle variations. Collecting measurements during the vapor plume generation from the melt pool further complicates the data extraction because of the poor visibility and short timescale between changing melt pool dynamics and spatter ejections. Harnessing the strength of high-fidelity 3D simulation and ML models, the slight variation in the properties can appear in patterns across measurements and be detected; aiding in differentiating the measured properties of both the melt pool and the spatter at ejections. Statistical distributions were generated to demonstrate this effect, as shown in Figures 7 and 8. The diagonal of the pairplot displays a plotted histogram showing the distribution of the property measurements. On the left-hand side of the diagonal are the kernel density estimate (KDE) plots showing the data density concentration, while on the right-hand side of the diagonal histogram are the scatter plots of the distribution. The histogram plots along the diagonal for most of the measured parameters suggest that the spatter has a wider spatial distribution, with its density spread over a larger range. The melt pool, on the other hand, shows a more concentrated spatial distribution, indicating a more localized phenomenon. A wider distribution was observed with respect to the spatial distributions (x , y , z) of the spatter compared to that of the melt pool on the histograms

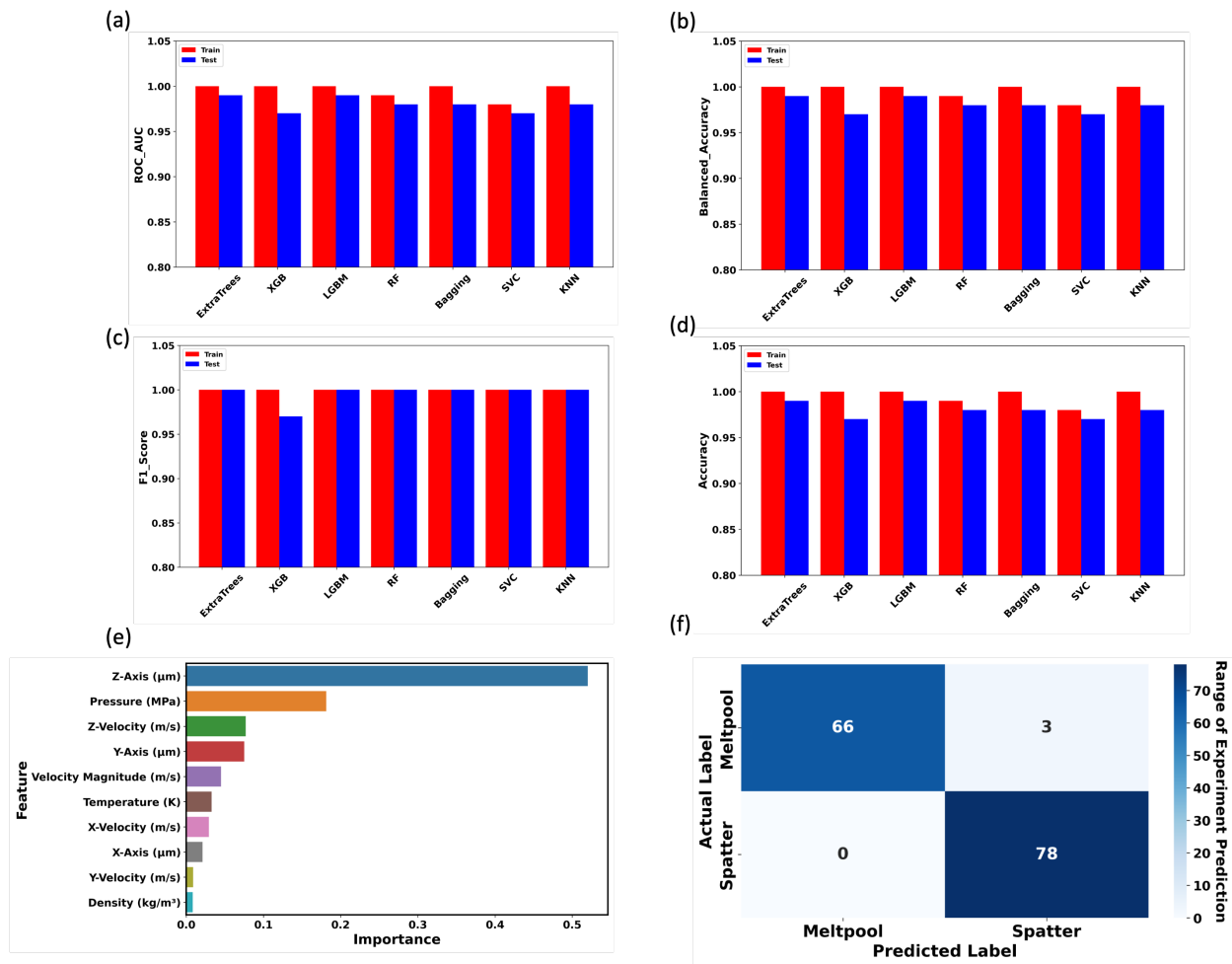


Figure 10: Performance measurement of ML models on classifying spatter ejection and melt pool with the following features: x-axis, y-axis, z-axis, temperature, velocity, x-velocity, y-velocity, z-velocity, density and pressure (a) ROC_AUC score (b) Balanced_Accuracy score (c) F1 score (d) Accuracy (e) Feature importance measurement from RF model (f) Quantification of the correct and wrong predictions of spatter and melt pool from RF model.

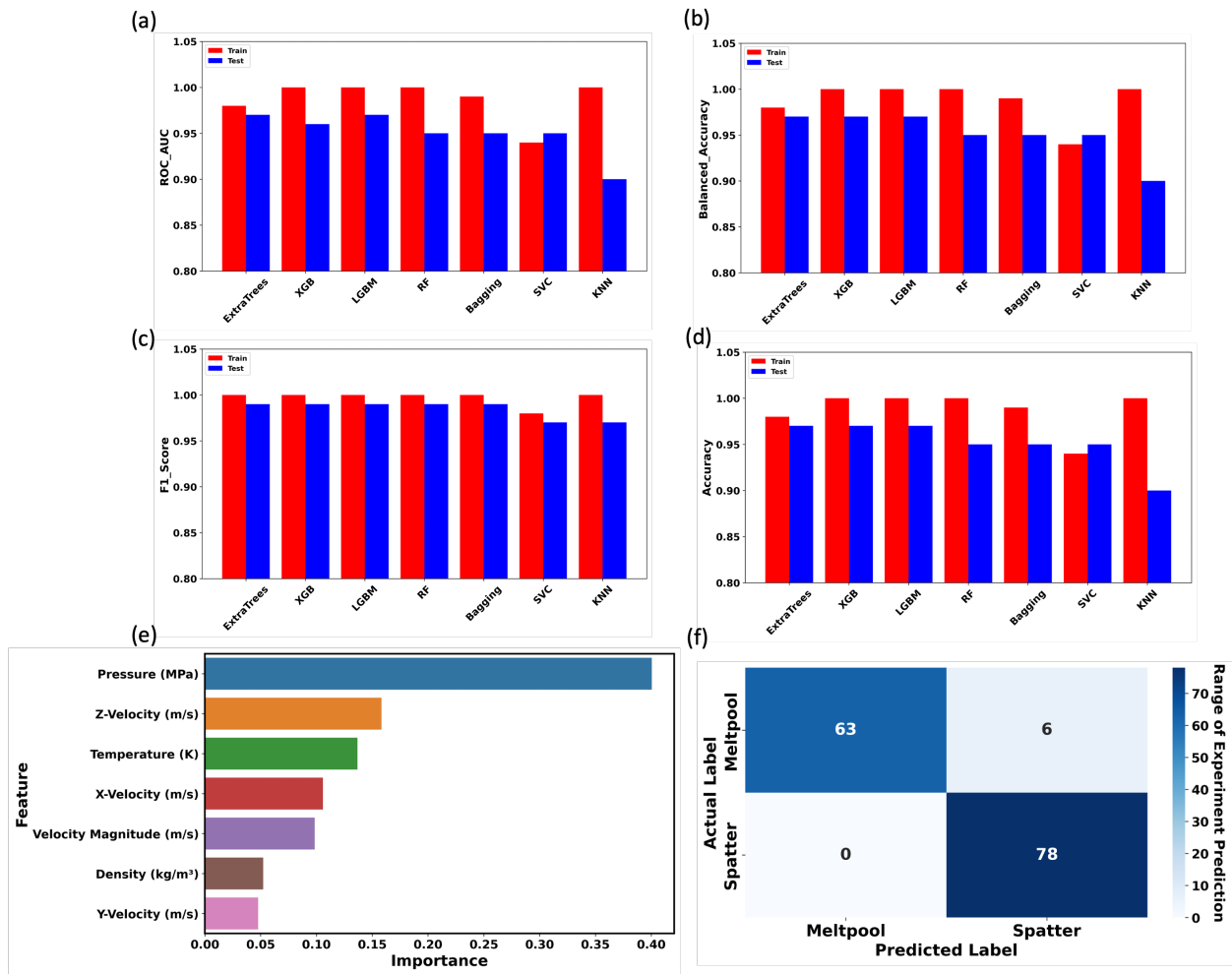


Figure 11: Performance measurement of ML models on classifying spatter ejection and melt pool with the following features: temperature, velocity, x-velocity, y-velocity, z-velocity, density and pressure (a) ROC_AUC score (b) Balanced_Accuracy score (c) F1 score (d) Accuracy (e) Feature importance measurement from RF model (f) Quantification of the correct and wrong predictions of spatter and melt pool from RF model.

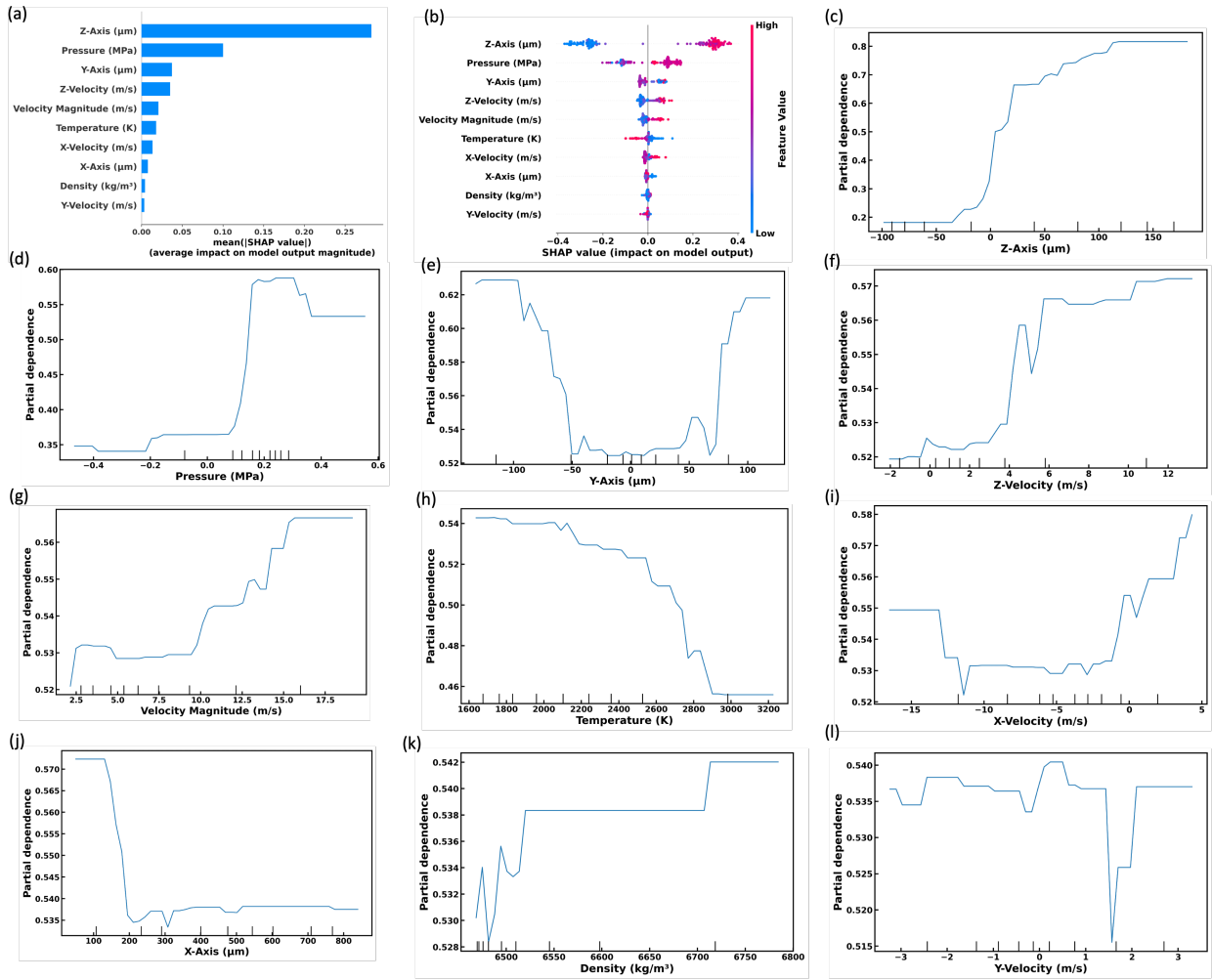


Figure 12: SHAP analysis on RF model in classifying spatter ejection and melt pool with the following features: temperature, velocity, x-velocity, y-velocity, z-velocity, density and pressure (a) SHAP feature important (b) The SHAP summary plot with a color bar (c) pressure PDP (d) z-velocity PDP (e) temperature PDP (f) x-velocity PDP (g) Velocity magnitude PDP (h) Density PDP (i) y-velocity PDP

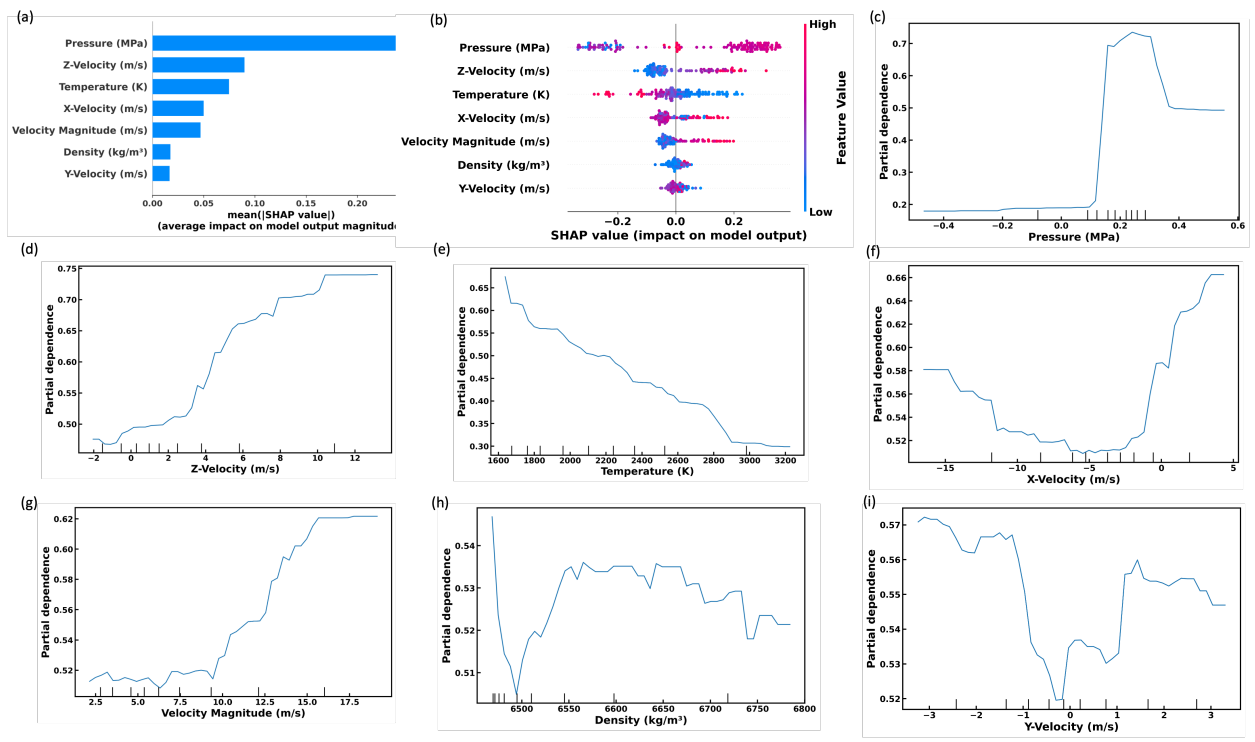


Figure 13: SHAP analysis on RF model in classifying spatter ejection and melt pool with the following features: temperature, velocity, x-velocity, y-velocity, z-velocity, density and pressure (a) SHAP feature important (b) Balanced_Accuracy score (c) z-axis PDP (d) pressure PDP (e) Partial dependence plot on y-axis PDP (f) z-velocity PDP (g) Velocity magnitude PDP (h) Temperature PDP (i) x-velocity PDP (j) x-axis PDP (k) Density PDP (l) y-velocity PDP

along the diagonal of the plot in Figure 7. The wider distribution can be attributed to the possibility that the ejection of the spatter is detected within and away from the location of the melt pool, which can depend on the velocity of the ejection and the simulation timestep. The wider spatial distribution of the spatter is more prominent along the y-axis. The circular shape of the laser beam can induce curvature growth of the melt pool, which, upon breaking, leads to spatter ejection and detection in the gas phase. The distance between the melt pool and the most ejected spatter is relatively short when compared to the size of the x-axis (laser traveling direction) and z-axis (simulation height) as shown in Figure 2. The scatter plot supports the prominence along the y-axis compared to the x and z axes. Consequently, a larger portion of the y-axis domain is likely to see the presence of spatter compared to the x-axis and the z-axis. A wider separation was observed between the histogram plot of the melt pool and the spatter along the z-axis, and it can be attributed to the spatter ejection being mostly occurring and detected at a height higher than that of the melt pool. For the velocity distributions shown in Figure 9, except for the y velocity, the KDE spatter plots, the histogram, and the scatter plots are broader, suggesting a wider range of velocities, while the melt pool plots are narrower, indicating more uniform velocities. y-velocity distributions appear to be similar with respect to the spatter and the melt pool, suggesting that y-velocity might be a weak parameter in driving spatter ejection. In addition, the density distributions between the spatter and the melt pool appear to be close to each other, with the spatter possessing a slightly broader distribution to the upper end, indicating evidence of cooling. Small amounts of spatter fall into this category, as shown in the scatter plot of density with respect to other parameters, indicating that most of the spatter are in the molten state as the melt pool. In general, spatter data points on the KDE plots, histogram, and scatter plots exhibit a wider spread, reinforcing the idea that spatter exhibits greater variability in spatial and velocity distributions, while melt pool shows tighter clustering.

In contrast, wider distribution spreads for the temperature and pressure of the melt pool

were observed compared to those observed for the spatter, implying a broader temperature and pressure range of the melt pool. Spatter shows higher peaks in the histogram plots, indicating that the temperatures are more consistent and concentrated around a mean value. The scatter plots for the spatter display more defined groupings, while the melt pool's points are dispersed over a wider range, confirming the trends suggested by the histogram plots. The melt pool pressure distribution is wider also, as indicated by its histogram and scatter plot, whereas the spatter exhibits a sharper peak. This suggests a narrow range of pressure values could be required for spatter ejections, assuming that the melt pool's pressure is close to the spatter's pressure at the point of ejection given the evidence of pressure overlap on the histogram plot. The scatter plots corresponding to the pressure of the melt pool against other parameters show a more dispersed pattern. The wider temperature and pressure distribution of the melt-pool data set is due to the high gradients of these properties along the melt-pool volume. Simultaneously, the narrower distribution of the spatter's temperature and pressure along with the reduced concentration at the upper bound compared to the melt pool could be due to its ejection occurring away from the laser impact on the material, resulting in cooling. The magnitude of cooling depends on the velocity of the ejection, especially when it travels away from the laser. In addition, the ejected spatter experiences pressure forces in all directions in the gas phase, causing an increase in the surface tension and the sphericity of their shape. Overall, the spatter represents a more variable and less controlled process with a broader range of values across most of the parameters, whereas the melt pool indicates a more stable and consistent process where the parameters are more narrowly distributed around certain central values. Spatter ejection from the melt pool could be attributed to the locations in the melt pool that possess the observed magnitude or threshold for the combination of parameters. However, it is crucial to quantify these parameters based on their importance to spatter generation.

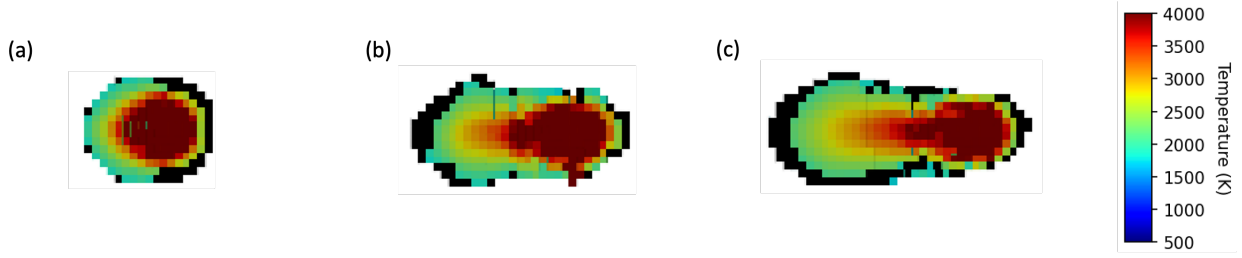


Figure 14: Spatter prediction on FLOW-3D simulation generated from testing FLOW-3D dataset at 400 W 2 m/s on ML model that was trained using OpenFOAM dataset. Region masked with black are identified as location predicted as spatter (a) prediction at timestep $65 \mu s$ (b) prediction at timestep $165 \mu s$ (c) prediction at timestep $265 \mu s$.

3.3. Spatter and Melt Pool Classification via ML Model.

To investigate the performance of the OpenFOAM data sets on ML models, features included the x-axis, y-axis, z-axis, temperature, velocity, x-velocity, y-velocity, z-velocity, density, and pressure are used as the model input. Consistently high accuracy was observed across all ML models, with training accuracy ranging from 98% to 100 % and testing accuracy ranging from 97% to 99%. The high accuracy was maintained across all calculated score metrics (Accuracy, F1, Balanced Accuracy, ROC_AUC) as shown in Figure 10(a-d) The lowest test accuracy of 97% was observed with the XGB and SVC models. The closeness of the training and testing accuracy indicates that the ML models are neither under- or over-fitting. The importance of the characteristics used in the ML test, as shown in 10e, followed the trend: z-axis > pressure > z-velocity > y-axis > temperature > velocity > x-velocity > y-velocity > density. The highest contribution of the z-axis to accuracy is attributed to the wide separation observed between the spatter and the melt pool when the z-axis is paired together with itself, or other parameters, as shown on the histogram, KDE, and scatter plots as shown in 7.

The methodologies of our data extraction and combination of parameters for this classification task is promising. These techniques can serve as a benchmark in predicting spatter or developing reduced order model package for spatter generation either with desired sim-

ulation packages or collected experimental measurements. Modeling LPBF in FLOW-3D generates a dataset that is well-suited for analyzing the melt pool rather than the spatter. Some parts of the melt pool dataset generated by FLOW-3D might have properties similar to those of spatter or meet the threshold required for spatter ejection. However, these locations remain part of the melt pool in the simulation because the physics module in FLOW-3D uses simplified assumptions for mass transfer between different phases, lacking the capability to accurately simulate spatter. Adapting the current ML model that was trained on OpenFOAM dataset will necessitate removal of spatial components (x, y, z) from the features that will be used to train and test ML models. On training and testing OpenFOAM dataset without spatial components, high accuracies were still achieved with slight decrease by 2% across the model performances in comparison to when spatial components were present as shown Figure 11. Significant decrease of 8 % was observe with the KNN model. The accuracy varies from 97 % to 95 % which are within the same range. High accuracy of the ML model with the features without spatial component qualify any one of the model for predicting spatter on FLOW-3D package. To ensure the models are not overfitting, we compared both the training and testing score as shown in the Figure 11. The largest difference between train and testing accuracy that was observed is 0.1 with respect to the KNN model, while the rest of the models are less than 0.05. These slight changes are small to consider the investigated model as not overfitting. The trend observed in the feature importance studies without spatial components, as shown in Figure 11e follows the trend of pressure > z-velocity > temperature > velocity > x-velocity > y-velocity > density. Evidently, pressure is not only the most significant parameter driving the dynamics in the melt pool, but also dictates possibility of spatter ejection as its magnitude is confined within a narrow range as shown in Figure 5. Strong importance observed with respect to z-velocity can be understood from the tendency of a body that possesses high z-velocity to travel upward, and we observed a narrow range for melt pool z-velocity, which is a subset of

spatter's z-velocity. Also, observing temperature having less importance than the z-velocity despite its direct relationship with pressure according to Clausius–Clapeyron relation could be attributed to the saturation that is reached such that increment in the temperature will result in boiling of the material which will not lead to spatter ejection, but more plume generation. In addition, Khairallah et al. [68] demonstrated the critical role of recoil pressure and Marangoni convection in shaping melt pool flow and influencing the formation of defects such as spattering, denudation, and pores. They found that as temperature rises, the recoil pressure increases, overcoming surface tension and generating depressions and spatter. High contribution of z-velocity to the spatter ejection could also be understood from the parabolic shape of the melt pool which is formed as the laser traverse in x-axis direction. Hot fluid will build up in the direction of the laser, which can break up to create spatter due to its elongation as shown in Figure 6a, via shear thinning. Additionally, spatter breakage can further intensify the backward dispersion of material and energy that are in form of a wave which can travel through the high gradient region of the melt pool, creating z-velocity component that could enhance ejection. The backward dispersion of material and energy in the melt pool can be attributed to the combination of other factors such as pressure, temperature gradient, and the vibration in the melt pool which can also influence other properties like viscosity and surface tension to cause Marangoni effect and promote melt pool flow, elongation and ultimately fluid ejections. To gain further insight to the distribution of ML model predictions, we constructed a precision recall table as shown on Figure 11f and 10f for predictions with spatial components included in the features and with no spatial components respectively. We observed our model having the capability in predicting most of the points with the melt pool and the spatter. The wrong prediction observations for the model with the presence of spatial component features and non-spatial component features is associated with regions that were melt pool but were falsely predicted as spatter and three and six respectively in number.

3.4. Explainable AI via SHAP Analysis.

The `shap.TreeExplainer` was used to calculate SHAP values for the test dataset, focusing on the contribution of features to the prediction of the positive class (spatter). Comparison of SHAP importance and ML importance ensures consistency in feature relevance across different methods. A summary bar plot was generated to visualize the mean absolute SHAP values, which indicate the average magnitude of feature impacts on the model's output. The SHAP summary bar plot offers a high-level overview of the importance of the features. Figure 12a and Figure 13a present the feature important from the SHAP analysis for the experiment with and without spatial components respectively, in the datasets. The x-axis represents the mean absolute SHAP values for each feature, indicating the average magnitude of a feature's impact on the model's output. Features are ranked in descending order, making it easy to identify the most influential features driving predictions. The SHAP feature importance rankings are consistent with the feature importance rankings derived directly from the ML model in Figure 10e and Figure 11e indicating consistency between the model's internal behavior and the SHAP explanation.

The SHAP summary plot with a color bar adds depth by visualizing the distribution of SHAP values for individual samples. Each point corresponds to a sample, with its position along the x-axis representing its SHAP value and its color encoding the feature value (e.g., high or low). This plot reveals both the importance and directionality of features, indicating patterns and interactions in the data. The farther the SHAP values deviate from zero, the stronger the influence of the feature on the model output, which was observed to follow the trends observed in 10b and Figure 11b. Furthermore, high values (red) are predominantly associated with positive SHAP values in high-influencing features such as Z-Axis, pressure, Z-Velocity, velocity magnitude, indicating their ability to increase the likelihood of spatter predictions. In reverse, a high value (red) of variable such as temperature and Y-axis tends to negative contributions to spatter generation.

To further understand the effect of changing the value of a particular feature on the prediction of the model, PDP plots were generated for each feature as shown on the Figure 12(c-l) and Figure 13(c-i). The y-axis of the PDP shows the average predicted probability of the positive class (spatter). In Figure 12c, we observed that the Z-Axis value has a significant threshold effect from $-10 \mu m$ to $40 \mu m$ suggesting this range is critical for the model's predictions, while beyond $100 \mu m$, the impact saturates. The extreme negative and positive values of the Y-axis strongly influence the model output, while values close to 0 have a minimal effect that indicates the symmetric behavior of the Y-axis to influence the predictions of the model with respect to the pressure (Figure 12d) and (Figure 13c), below 0.2 MPa, the partial dependence remains flat, indicating negligible impact on predictions. A sharp increase in partial dependence is observed as the pressure increases from approximately 0.1 to 0.2 MPa, where a significant positive impact is observed on the model predictions. The partial dependence is nearly flat and stable around 0.35, indicating that pressure in this range has minimal influence on the model's predictions. The curve plateaus around 0.55 to 0.60, suggesting that increasing pressure beyond this point does not have a substantial additional impact on the predictions. A significant increase in Z velocity was observed from 2 m/s to 5 m/s (Figure 12f), while the velocity magnitude initially increased at 2.5 m/s, then almost stabilized to 10 m/s where it continued to increase to 17 m/s (Figure 12 g). Close partner was observed in the PDP plot of features with the ML experiment, where there are no spatial components in the input features in Figure 13. Steady reduction in temperature was observed to favor spatter generation (Figure 12h and Figure 13e) which could be attributed to spatter generation occurring mostly away from the location of the laser, as the fluid swirl backward due to the Marangoni recirculation effect. Along the X-Axis (the laser traveling direction) in Figure 12j, SHAP value decline at the initial stage then remain almost steady at the higher value X-Axis. Although the SHAP values of features like Y-Velocity, density, and X-Axis are small, it is likely that they promote the accuracy

predictions in our studies due to their tendency to interact with features with high SHAP values.

3.5. Spatter Prediction on a Commercial Package "FLOW-3D".

Spatter prediction on FLOW-3D is promoted by two factors: (1) the close alignment between the characteristics of the melting pool dimensions and the temperature distribution of OpenFOAM and FLOW-3D and (2) the high precision of the ML model in classifying the spatter from the melting pool. Upon testing our model on FLOW-3D, voxels that match the spatter property were identified and masked with black points as shown in Figure 14. At the early timesteps of the FLOW-3D simulation, spatter predictions were predominantly observed at the front of the melt pool (Figure 14a), then at the last time steps (Figure 14b and Figure 14c), the spatter tends to occupy the backward side of the melt pool, this is similar to the observed OpenFOAM simulation for spatter generation as shown in Figure 9 and the experimental result reported by Yin et al. [5]. Note that conditions for spatter generation were not met at the location of the hotspot of the melt pool because of the high temperature that could be causing fluid evaporation. Consequently, the high accuracy outcome of the Random Forest (RF) model underscores the efficacy of our developed methodology for the reduced order task. This methodology can enhance the robustness of commercial packages by synergizing them with machine learning (ML) models to account for complex and computationally expensive phenomena, such as spatter modeling. An alternative application of the developed methodology is testing datasets of different process parameters generated from commercial software, such as FLOW-3D, towards the development of a process map.

3.6. Spatter Process Map

Display of spatter quantification with varying power/velocity combinations will provide access to a suitable operating window with minimal defects for part production. Running OpenFOAM for additive manufacturing is computationally expensive due to a lack of sim-

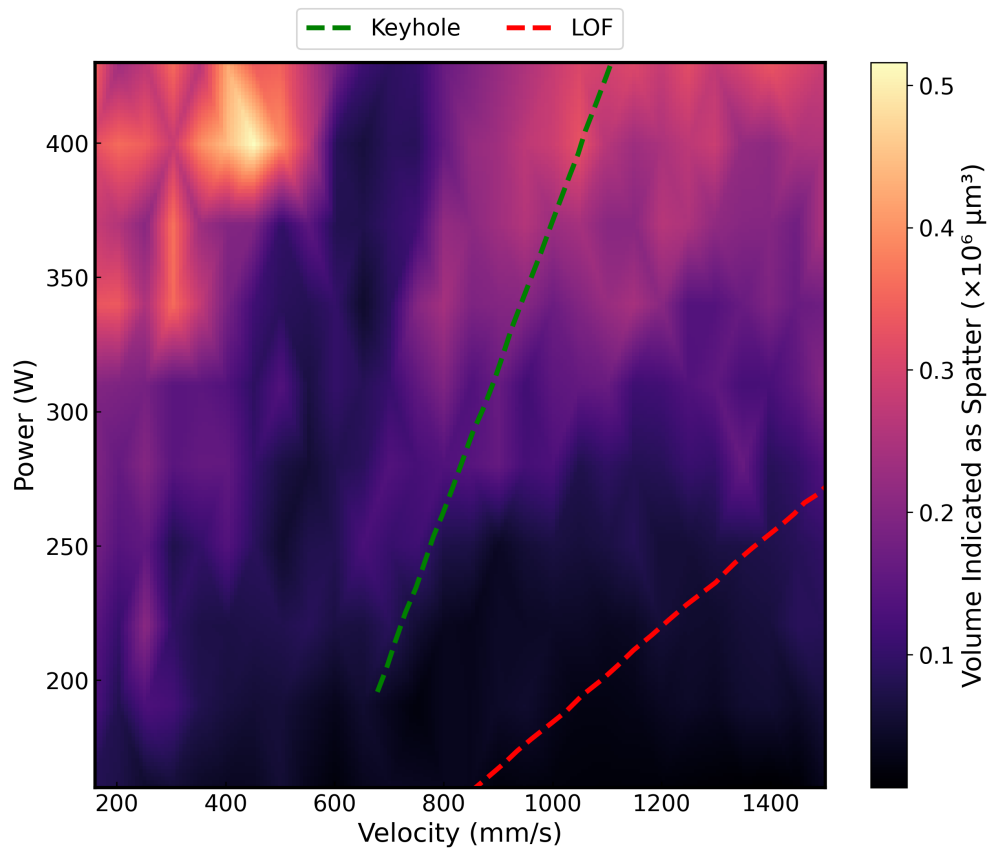


Figure 15: Process map generated via hybrid of OpenFOAM trained ML model on FLOW-3D dataset to understand relationship between spatter formation and process conditions. The process map was created using 283 FLOW-3D simulations with different combinations of power and velocity.

plifying assumptions in the physics it is configured to solve as compared to FLOW-3D, that has a devoted module for AM. On the same machine, both FLOW-3D and OpenFOAM require run times of 4 and 72 hours respectively to generate LPBF solution on $5 \mu m$ mesh size using Intel(R)Xeon(R) Gold 6230R CPU @ 2.10GHz, 2095Mhz, 26 cores. Building a hybrid of OpenFOAM and FLOW-3D via the high accuracy ML model as a reduced order model is attractive for large dataset generation for the development of spatter process map. Figure 15 is generated by testing 281 dataset consisting varying power/velocity combinations of FLOW-3D experiments on OpenFOAM trained ML model. The red and green lines overlay on the plot are extracted from a previous study on porosity by Rollett et al. [12] indicating boundary within which keyhole and lack of fusion (LOF) respectively were prominent. In-between the boundary is the window identify as process window where keyhole and LOF are minimal. These lines are overlaid on the spatter count process map to relate the generated spatter count at a specific power/velocity combination to the nature of porosity that is likely to be present with the aim of identifying region on the process map where minimal effect of porosity and spatter can be seen during part building. As shown in Figure 15, the spatter quantification follows a predictable trend within processing parameter space for LPBF, except in a region between $500 - 700 \text{ mms}^{-1}$ where spatter count is consistently low across the power range investigated. This is also clearly demonstrated in Figures A.11 and A.12 of the Appendix. It was observed that higher spatter was generated at high power and low velocity, which is the region associated with keyhole formation. Conversely, at low power and high speed, less spatter was observed, corresponding to the region characterized by lack of fusion [12]. Based on the process conditions, we observed the trend followed by the volume of spatter generation as high power/low speed $>$ high power/high speed $>$ low power/low speed $>$ low power/high speed. The observed trend can be attributed to the intensity of the interaction between the material and the laser, leading to variations in melt pool size, and the magnitude of mass and energy transport. Consequently, high power and

low velocity produce the largest melt pool with the most intense transport phenomena and kinetic effects, resulting in the highest spatter ejection. In contrast, low power and high velocity create the smallest melt pool with the least intense effects, resulting in minimal spatter ejection. Certain locations within the safe operating window for porosity (situated between keyhole formation and lack of fusion) [12] intersect with areas of low spatter count, as shown in Figure 9. These intersections make those regions promising for part printing. The reason for the observed low spatter volume at a velocity between 500 - 700 *mm/s* throughout the investigated power range is probably the transition between a kinetic regime and a diffusion-limited regime resulting from a change in the morphology of the melt pool. This transition creates a balanced environment in which the dynamics of the melt pool is stabilized, leading to reduced ejection of spatters due to moderate vaporization, stable formation of the melt pool, and efficient heat distribution.

The analysis of the study by Zheng et al. [69] further supports the transition observed on the process map from 400 - 700 *mm/s*. They examined the formation and evolution of the plume and its impact on the generation of spatter in stainless steel at varying scan speeds. (200 *mm/s*, 400 *mm/s*, 500 *mm/s*, 1000 *mm/s*, and 2000 *mm/s*). They believe that spatter generation is more likely to depend on the stability of the plume throughout the experiments. They discovered that at lower scan speeds (200 *mm/s*), the vapor plume was highly unstable because of the high energy density, with recoil pressure strong enough to eject droplets from the melt pool. As the laser scan speed increased to 400 – 500 *mm/s*, spattering and plume formation barely occurred. Further increasing the speed to 1000 *mm/s* and 2000 *mm/s* caused the melt track to become unstable, showing periodic swelling connected by narrow bottlenecks of ripples along the melt track, a result of the Plateau-Rayleigh capillary instability [70]. When the scan speed exceeds a certain threshold (500 *mm/s* in our study), the vapor plume tilts backward relative to the scan direction. This tilt is believed to result from a shift in the laser-material interaction interface from the bottom to the front wall of

the depression or keyhole. The resulting backward vapor flux is thought to further influence the fluid dynamics within the melt pool, increasing the susceptibility of the melt track's end to open-pore formation.

4. Conclusion

In this work, we developed multiphysics simulation of a single-track selective laser melting using OpenFOAM, which has the capability to produce the 3D high resolution properties of spatter and melt pool dynamics. In addition, a tracking algorithm was developed to extract the data set used to characterize spatter ejection, the melt pool, and to perform ML classification tasks. Upon screening our datasets using different machine learning models such as ExtraTrees, XGB, LGBM, RF, Bagging, SVC and KNN, we observed high accuracy greater than 97 % for all the ML models implemented. Upon removing the spatial component (x, y, z) from the OpenFOAM data set used to train / test the ML model to match the accessible data set that can be extracted from FLOW-3D, we high accuracy ranging from 95 % to 97 % were achieved across the investigated model expect KNN which has the lowest value of 90 %. The high accuracy result of ML predictions underscores the efficacy of our ML models in exploring the model for the reduced-order task of spatter prediction, by rigorously testing datasets from the commercial software. The regions associated with spatter in the FLOW-3D simulation output were predicted and visualized on a voxel-by-voxel basis. LPBF melt pool simulations are significantly faster on FLOW-3D than OpenFOAM, LPBF melt pool simulations are significantly faster on FLOW-3D than on OpenFOAM. This makes the screening of a large number of process parameters collected from FLOW-3D feasible. Using an ML model trained on the OpenFOAM dataset, we can develop a process map that displays spatter trends in a large process parameter space. Correlation of the possible amount of spatter with changing power/velocity combination was generated. It was observed that at a high power and low laser speed, more spatters were generated in comparison to

low power and high speed.

Declarations

Funding

This research was sponsored by the Army Research Laboratory and conducted under Cooperative Agreement Number W911NF-20-2-0175. The views and conclusions presented in this document are those of the authors and do not necessarily represent the official policies or positions of the Army Research Laboratory or the U.S. Government. The U.S. Government is authorized to reproduce and distribute reprints for governmental purposes, despite any copyright notice herein.

Competing Interests

The authors have no competing interests to declare that are relevant to the content of this article.

References

- [1] Florian Wirth, Teresa Tonn, Markus Schöberl, Stefan Hermann, Hannes Birkhofer, and Vasily Ploshikhin. Implementation of the marangoni effect in an open-source software environment and the influence of surface tension modeling in the mushy region in laser powder bed fusion (lpbf). *Modelling and Simulation in Materials Science and Engineering*, 30(3):034001, 2022.
- [2] Giulia Repossini, Vittorio Laguzza, Marco Grasso, and Bianca Maria Colosimo. On the use of spatter signature for in-situ monitoring of laser powder bed fusion. *Additive Manufacturing*, 16:35–48, 2017.
- [3] Ross Cunningham, Sneha P Narra, Colt Montgomery, Jack Beuth, and AD Rollett. Synchrotron-based x-ray microtomography characterization of the effect of processing variables on porosity formation in laser power-bed additive manufacturing of ti-6al-4v. *Jom*, 69:479–484, 2017.
- [4] Chinnapat Panwisawas, Yuanbo T Tang, and Roger C Reed. Metal 3d printing as a disruptive technology for superalloys. *Nature Communications*, 11(1):2327, 2020.

- [5] Jie Yin, Dengzhi Wang, Liangliang Yang, Huiliang Wei, Peng Dong, Linda Ke, Guoqing Wang, Haihong Zhu, and Xiaoyan Zeng. Correlation between forming quality and spatter dynamics in laser powder bed fusion. *Additive Manufacturing*, 31:100958, 2020.
- [6] Zheng Li, Hao Li, Jie Yin, Yan Li, Zhenguo Nie, Xiangyou Li, Deyong You, Kai Guan, Wei Duan, Longchao Cao, et al. A review of spatter in laser powder bed fusion additive manufacturing: In situ detection, generation, effects, and countermeasures. *Micromachines*, 13(8):1366, 2022.
- [7] S Mohammad H Hojjatzadeh, Niranjana D Parab, Qilin Guo, Minglei Qu, Lianghua Xiong, Cang Zhao, Luis I Escano, Kamel Fezzaa, Wes Everhart, Tao Sun, et al. Direct observation of pore formation mechanisms during lpbf additive manufacturing process and high energy density laser welding. *International Journal of Machine Tools and Manufacture*, 153:103555, 2020.
- [8] Aiden A Martin, Nicholas P Calta, Saad A Khairallah, Jenny Wang, Phillip J Depond, Anthony Y Fong, Vivek Thampy, Gabe M Guss, Andrew M Kiss, Kevin H Stone, et al. Dynamics of pore formation during laser powder bed fusion additive manufacturing. *Nature communications*, 10(1):1987, 2019.
- [9] T Mukherjee and Tarasankar DebRoy. Mitigation of lack of fusion defects in powder bed fusion additive manufacturing. *Journal of Manufacturing Processes*, 36:442–449, 2018.
- [10] Patcharapit Promoppatum, Raghavan Srinivasan, Siu Sin Quek, Sabeur Msolli, Shashwat Shukla, Nur Syafiqah Johan, Sjoerd van der Veen, and Mark Hyunpong Jhon. Quantification and prediction of lack-of-fusion porosity in the high porosity regime during laser powder bed fusion of ti-6al-4v. *Journal of Materials Processing Technology*, 300:117426, 2022.
- [11] Zhongshu Ren, Lin Gao, Samuel J Clark, Kamel Fezzaa, Pavel Shevchenko, Ann Choi, Wes Everhart, Anthony D Rollett, Lianyi Chen, and Tao Sun. Machine learning–aided real-time detection of keyhole pore generation in laser powder bed fusion. *Science*, 379(6627):89–94, 2023.
- [12] Jerard V Gordon, Sneha P Narra, Ross W Cunningham, He Liu, Hangman Chen, Robert M Suter, Jack L Beuth, and Anthony D Rollett. Defect structure process maps for laser powder bed fusion additive manufacturing. *Additive Manufacturing*, 36:101552, 2020.
- [13] Zachary A Young, Qilin Guo, Niranjana D Parab, Cang Zhao, Minglei Qu, Luis I Escano, Kamel Fezzaa, Wes Everhart, Tao Sun, and Lianyi Chen. Types of spatter and their features and formation mechanisms in laser powder bed fusion additive manufacturing process. *Additive Manufacturing*, 36:101438, 2020.
- [14] Ahmad Bin Anwar and Quang-Cuong Pham. Study of the spatter distribution on the powder bed during selective laser melting. *Additive Manufacturing*, 22:86–97, 2018.
- [15] Zhiqiang Wang, Xuede Wang, Xin Zhou, Guangzhao Ye, Xing Cheng, and Peiyu Zhang. Investigation

- into spatter particles and their effect on the formation quality during selective laser melting processes. *CMES-Computer Modeling in Engineering & Sciences*, 124(1), 2020.
- [16] Katayoon Taherkhani, Esmat Sheydaeian, Christopher Eischer, Martin Otto, and Ehsan Toyserkani. Development of a defect-detection platform using photodiode signals collected from the melt pool of laser powder-bed fusion. *Additive Manufacturing*, 46:102152, 2021.
- [17] Shuhao Wang, Jinsheng Ning, Lida Zhu, Zhichao Yang, Wentao Yan, Yichao Dun, Pengsheng Xue, Peihua Xu, Susmita Bose, and Amit Bandyopadhyay. Role of porosity defects in metal 3d printing: Formation mechanisms, impacts on properties and mitigation strategies. *Materials Today*, 2022.
- [18] Ross Cunningham, Cang Zhao, Niranjana Parab, Christopher Kantzos, Joseph Pauza, Kamel Fezzaa, Tao Sun, and Anthony D Rollett. Keyhole threshold and morphology in laser melting revealed by ultrahigh-speed x-ray imaging. *Science*, 363(6429):849–852, 2019.
- [19] Sonny Ly, Alexander M Rubenchik, Saad A Khairallah, Gabe Guss, and Manyalibo J Matthews. Metal vapor micro-jet controls material redistribution in laser powder bed fusion additive manufacturing. *Scientific reports*, 7(1):4085, 2017.
- [20] Zackary Snow, Luke Scime, Amirkoushyar Ziabari, Brian Fisher, and Vincent Paquit. Observation of spatter-induced stochastic lack-of-fusion in laser powder bed fusion using in situ process monitoring. *Additive Manufacturing*, 61:103298, 2023.
- [21] Reza Esmaeilizadeh, Usman Ali, Ali Keshavarzkermani, Yahya Mahmoodkhani, Ehsan Marzbanrad, and Ehsan Toyserkani. On the effect of spatter particles distribution on the quality of hastelloy x parts made by laser powder-bed fusion additive manufacturing. *Journal of Manufacturing Processes*, 37:11–20, 2019.
- [22] Florian Wirth, Alex Frauchiger, Kai Gutknecht, and Michael Cloots. Influence of the inert gas flow on the laser powder bed fusion (lpbf) process. In *Industrializing Additive Manufacturing: Proceedings of AMPA2020*, pages 192–204. Springer, 2021.
- [23] Mohsen Taheri Andani, Reza Dehghani, Mohammad Reza Karamooz-Ravari, Reza Mirzaeifar, and Jun Ni. Spatter formation in selective laser melting process using multi-laser technology. *Materials & Design*, 131:460–469, 2017.
- [24] Christopher Barrett, Carolyn Carradero, Evan Harris, Jeremy McKnight, Jason Walker, Eric MacDonald, and Brett Conner. Low cost, high speed stereovision for spatter tracking in laser powder bed fusion. In *2018 International Solid Freeform Fabrication Symposium*. University of Texas at Austin, 2018.

- [25] Nicholas O'Brien, Syed Zia Uddin, Jordan Weaver, Jake Jones, Satbir Singh, and Jack Beuth. Computational analysis and experiments of spatter transport in a laser powder bed fusion machine. *Additive Manufacturing*, page 104133, 2024.
- [26] Christopher Barrett, Carolyn Carradero, Evan Harris, Kirk Rogers, Eric MacDonald, and Brett Conner. Statistical analysis of spatter velocity with high-speed stereovision in laser powder bed fusion. *Progress in Additive Manufacturing*, 4(4):423–430, 2019.
- [27] Hiroshi Nakamura, Yousuke Kawahito, Koji Nishimoto, and Seiji Katayama. Elucidation of melt flows and spatter formation mechanisms during high power laser welding of pure titanium. *Journal of Laser Applications*, 27(3), 2015.
- [28] Minglei Qu, Qilin Guo, Luis I Escano, Ali Nabaa, S Mohammad H Hojjatzadeh, Zachary A Young, and Lianyi Chen. Controlling process instability for defect lean metal additive manufacturing. *Nature communications*, 13(1):1079, 2022.
- [29] Shengjie Deng, Hui-Ping Wang, Fenggui Lu, Joshua Solomon, and Blair E Carlson. Investigation of spatter occurrence in remote laser spiral welding of zinc-coated steels. *International Journal of Heat and Mass Transfer*, 140:269–280, 2019.
- [30] OpenCFD Ltd (ESI Group). Openfoam documentation. (online) <https://www.openfoam.com/documentation/overview>).
- [31] OpenCFD Ltd (ESI Group). Openfoam news. (online) <https://www.openfoam.com/news/main-news/openfoam-v20-12>).
- [32] Francis Ogoke, William Lee, Ning-Yu Kao, Alexander Myers, Jack Beuth, Jonathan Malen, and Amir Barati Farimani. Convolutional neural networks for melt depth prediction and visualization in laser powder bed fusion. *The International Journal of Advanced Manufacturing Technology*, 129(7):3047–3062, 2023.
- [33] XIA Yang, Suhaib Zafar, J-X Wang, and Heng Xiao. Predictive large-eddy-simulation wall modeling via physics-informed neural networks. *Physical Review Fluids*, 4(3):034602, 2019.
- [34] Francis Ogoke, Quanliang Liu, Olabode Ajenifujah, Alexander Myers, Guadalupe Quirarte, Jack Beuth, Jonathan Malen, and Amir Barati Farimani. Inexpensive high fidelity melt pool models in additive manufacturing using generative deep diffusion. *arXiv preprint arXiv:2311.16168*, 2023.
- [35] Chengcheng Wang, XP Tan, Shu Beng Tor, and CS Lim. Machine learning in additive manufacturing: State-of-the-art and perspectives. *Additive Manufacturing*, 36:101538, 2020.
- [36] Emmanuel Stathatos and George-Christopher Vosniakos. Real-time simulation for long paths in laser-

- based additive manufacturing: a machine learning approach. *The International Journal of Advanced Manufacturing Technology*, 104:1967–1984, 2019.
- [37] Yayati Jadhav, Joseph Berthel, Chunshan Hu, Rahul Panat, Jack Beuth, and Amir Barati Farimani. Stressd: 2d stress estimation using denoising diffusion model. *Computer Methods in Applied Mechanics and Engineering*, 416:116343, 2023.
- [38] Sofia Sheikh, Brent Vela, Vahid Attari, Xueqin Huang, Peter Morcos, James Hanagan, Cafer Acemi, Ibrahim Karaman, Alaa Elwany, and Raymundo Arroyave. Exploring chemistry and additive manufacturing design spaces: a perspective on computationally-guided design of printable alloys. *Materials Research Letters*, 12(4):235–263, 2024.
- [39] Xiling Yao, Seung Ki Moon, and Guijun Bi. A hybrid machine learning approach for additive manufacturing design feature recommendation. *Rapid Prototyping Journal*, 23(6):983–997, 2017.
- [40] Martin P Bendsoe, Erik Lund, Niels Olhoff, and Ole Sigmund. Topology optimization-broadening the areas of application. *Control and Cybernetics*, 34(1):7–35, 2005.
- [41] Parand Akbari, Francis Ogoke, Ning-Yu Kao, Kazem Meidani, Chun-Yu Yeh, William Lee, and Amir Barati Farimani. Melpoolnet: Melt pool characteristic prediction in metal additive manufacturing using machine learning. *Additive Manufacturing*, 55:102817, 2022.
- [42] Omid Barati Farimani, Zhonglin Cao, and Amir Barati Farimani. Fast water desalination with a graphene–mos2 nanoporous heterostructure. *ACS Applied Materials & Interfaces*, 16(22):29355, 2024.
- [43] AmirPouya Hemmasian, Francis Ogoke, Parand Akbari, Jonathan Malen, Jack Beuth, and Amir Barati Farimani. Surrogate modeling of melt pool temperature field using deep learning. *Additive Manufacturing Letters*, 5:100123, 2023.
- [44] Yang Du, Tuhin Mukherjee, and Tarasankar DebRoy. Physics-informed machine learning and mechanistic modeling of additive manufacturing to reduce defects. *Applied Materials Today*, 24:101123, 2021.
- [45] Di Wang, Yongqiang Yang, Yang Liu, Yuchao Bai, and Chaolin Tan. Formation mechanism of spatter and its influence on mechanical properties in process of laser powder bed fusion. In *Laser Powder Bed Fusion of Additive Manufacturing Technology*, pages 135–177. Springer, 2023.
- [46] Peter S Cook and Anthony B Murphy. Simulation of melt pool behaviour during additive manufacturing: Underlying physics and progress. *Additive Manufacturing*, 31:100909, 2020.
- [47] Bo Cheng, Lukas Loeber, Hannes Willeck, Udo Hartel, and Charles Tuffile. Computational investigation of melt pool process dynamics and pore formation in laser powder bed fusion. *Journal of Materials*

- Engineering and Performance*, 28:6565–6578, 2019.
- [48] Jennifer Lundkvist. Cfd simulation of fluid flow during laser metal wire deposition using openfoam: 3d printing, 2019.
- [49] J U Brackbill, D B Kothe, and C Zemach. A continuum method for modeling surface tension. *J. Comput. Phys.*, 100:335–354, 1992.
- [50] Gregor Cerne, Stojan Petelin, and Iztok Tiselj. Coupling of the interface tracking and the two-fluid models for the simulation of incompressible two-phase flow. *Journal of computational physics*, 171(2):776–804, 2001.
- [51] Zaki Saptari Saldi. Marangoni driven free surface flows in liquid weld pools. *Delft University of Technology, The Netherlands*, 2012.
- [52] Alexander Klassen, Thorsten Scharowsky, and Carolin Körner. Evaporation model for beam based additive manufacturing using free surface lattice boltzmann methods. *Journal of Physics D: Applied Physics*, 47(27):275303, 2014.
- [53] Hyungson Ki, Jyoti Mazumder, and Pravansu S Mohanty. Modeling of laser keyhole welding: Part i. mathematical modeling, numerical methodology, role of recoil pressure, multiple reflections, and free surface evolution. *Metallurgical and materials transactions A*, 33:1817–1830, 2002.
- [54] Thorsten Heeling, Michael Cloots, and Konrad Wegener. Melt pool simulation for the evaluation of process parameters in selective laser melting. *Additive Manufacturing*, 14:116–125, 2017.
- [55] Liu Cao. Mesoscopic-scale simulation of pore evolution during laser powder bed fusion process. *Computational Materials Science*, 179:109686, 2020.
- [56] Mohammad Bahreini, Abbas Ramiar, and Ali Akbar Ranjbar. Development of a phase change model for volume-of-fluid method in openfoam. *Journal of Heat and Mass Transfer Research*, 3(2):131–143, 2016.
- [57] Wen Ho Lee. A pressure iteration scheme for two-phase flow modeling. *Multiphase transport fundamentals, reactor safety, applications*, 1:407–431, 1980.
- [58] NL Scuro, M Poschmann, O Beneš, and MHA Piro. Progress in coupling computational thermodynamics and computational fluid dynamics to support molten salt reactor applications. In *Conference Paper: G4SR4*, pages 1–15, 2022.
- [59] Bochuan Liu, Ricky Wildman, Christopher Tuck, Ian Ashcroft, and Richard Hague. Investigation the effect of particle size distribution on processing parameters optimisation in selective laser melting process. 2011.

- [60] Zachary Young, Minglei Qu, Meelap Michael Coday, Qilin Guo, Seyed Mohammad H Hojjatzadeh, Luis I Escano, Kamel Fezzaa, and Lianyi Chen. Effects of particle size distribution with efficient packing on powder flowability and selective laser melting process. *Materials*, 15(3):705, 2022.
- [61] V Bobkov, L Fokin, E Petrov, V Popov, V Rumiantsev, and A Savvatimsky. Thermophysical properties of materials for nuclear engineering: a tutorial and collection of data. *IAEA, Vienna*, pages 18–21, 2008.
- [62] Alexander J Myers, Guadalupe Quirarte, Francis Ogoke, Brandon M Lane, Syed Zia Uddin, Amir Barati Farimani, Jack L Beuth, and Jonathan A Malen. High-resolution melt pool thermal imaging for metals additive manufacturing using the two-color method with a color camera. *Additive Manufacturing*, 73:103663, 2023.
- [63] Christophe Fiorio and Jens Gustedt. Two linear time union-find strategies for image processing. *Theoretical Computer Science*, 154(2):165–181, 1996.
- [64] Bernard A Galler and Michael J Fisher. An improved equivalence algorithm. *Communications of the ACM*, 7(5):301–303, 1964.
- [65] Stéfan van der Walt, Johannes L. Schönberger, Juan Nunez-Iglesias, François Boulogne, Joshua D. Warner, Neil Yager, Emmanuelle Gouillart, Tony Yu, and the scikit-image contributors. scikit-image: image processing in Python. *PeerJ*, 2:e453, 6 2014.
- [66] Scott Lundberg. A unified approach to interpreting model predictions. *arXiv preprint arXiv:1705.07874*, 2017.
- [67] Pierre Geurts, Damien Ernst, and Louis Wehenkel. Extremely randomized trees. *Machine learning*, 63(1):3–42, 2006.
- [68] Saad A Khairallah, Andrew T Anderson, Alexander Rubenchik, and Wayne E King. Laser powder-bed fusion additive manufacturing: Physics of complex melt flow and formation mechanisms of pores, spatter, and denudation zones. *Acta Materialia*, 108:36–45, 2016.
- [69] Hang Zheng, Huaixue Li, Lihui Lang, Shuili Gong, and Yulong Ge. Effects of scan speed on vapor plume behavior and spatter generation in laser powder bed fusion additive manufacturing. *Journal of Manufacturing Processes*, 36:60–67, 2018.
- [70] Saad A Khairallah and Andy Anderson. Mesoscopic simulation model of selective laser melting of stainless steel powder. *Journal of Materials Processing Technology*, 214(11):2627–2636, 2014.
- [71] Leo Breiman. Random forests. *Machine learning*, 45(1):5–32, 2001.
- [72] Hussam Safieh, Rami A Hawileh, Maha Assad, Rawan Hajjar, Sayan Kumar Shaw, and Jamal Ab-

- dalla. Using multiple machine learning models to predict the strength of uhpc mixes with various fa percentages. *Infrastructures*, 9(6):92, 2024.
- [73] Leo Breiman. Bagging predictors. *Machine learning*, 24(2):123–140, 1996.
- [74] Corinna Cortes and Vladimir Vapnik. Support-vector networks. *Machine learning*, 20(3):273–297, 1995.
- [75] Gyulim Kim and Seungku Kim. A road defect detection system using smartphones. *Sensors*, 24(7):2099, 2024.
- [76] Arthur E. Hoerl and Robert W. Kennard. Ridge regression: Biased estimation for nonorthogonal problems. *Technometrics*, 12(1):55–67, 1970.
- [77] Youssef Hbali, Sara Hbali, Lahoucine Ballihi, and Mohammed Sadgal. Skeleton-based human activity recognition for elderly monitoring systems. *IET Computer Vision*, 12(1):16–26, 2018.
- [78] Mohammed Alser, Taha Shahroodi, Juan Gómez-Luna, Can Alkan, and Onur Mutlu. Sneakysnake: a fast and accurate universal genome pre-alignment filter for cpus, gpus and fpgas. *Bioinformatics*, 36(22-23):5282–5290, 2020.
- [79] Tianqi Chen and Carlos Guestrin. Xgboost: A scalable tree boosting system. In *Proceedings of the 22nd acm sigkdd international conference on knowledge discovery and data mining*, pages 785–794, 2016.
- [80] Mingeun Son, Gangpyo Lee, Jaeyong Park, and Min Choi. Design and implementation of health and risk level assessment for socially disadvantaged patients. *Applied Sciences*, 13(21):12014, 2023.
- [81] Guolin Ke, Qi Meng, Thomas Finley, Taifeng Wang, Wei Chen, Weidong Ma, Qiwei Ye, and Tie-Yan Liu. Lightgbm: A highly efficient gradient boosting decision tree. In *Advances in neural information processing systems*, pages 3146–3154, 2017.

Appendix A. Machine Learning Models

Appendix A.0.1. Random Forest Classifier (RFClassifier)

Random Forest Classifier is an ensemble learning method that builds numerous decision trees during training and outputs the class that is the most frequent among the individual trees' predictions [71]. Random forests help mitigate the tendency of the decision trees to overfit their training data [72].

Appendix A.0.2. BaggingClassifier

BaggingClassifier is a meta-estimator ensemble learning method that trains base classifiers on random subsets of the original dataset and then combines their individual predictions to produce a final prediction. [73]. This approach helps to minimize the model's variance as it combines multiple learners' strengths and smooths out their predictions.

Appendix A.0.3. Support Vector Classifier (SVC)

Support Vector Classifier (SVC) is a powerful, flexible, and robust model for classification tasks [74]. It introduced the concept of decision planes to establish decision boundaries. SVC seeks to identify a decision plane that optimizes the margin among different classes in the training set, making it particularly well-suited for binary classification problems [75].

Appendix A.1. Ridge Linear Regression (Ridge)

Ridge regression is a regularized version of linear regression, used to reduce overfitting which can occur when the model is over-specified for a small dataset [76]. This method performs L_2 regularization. Ridge regression shrinks the parameters by imposing a constraint on their values, helping to reduce the model complexity and overfitting.

Appendix A.2. The Extra Trees Classifier (Extremely Randomized Trees)

The Extra Trees Classifier (Extremely Randomized Trees) is an ensemble learning method fundamentally similar to Random Forests [67]. However, it differs in the way it constructs the

trees. In Extra Trees, randomness is taken a step further in how the splits are determined. In the tree learner, the top-down splitting process is randomized. Instead of calculating the most effective thresholds, thresholds are selected randomly, and the best from the randomly chosen thresholds is used for the splitting rule [77]. This resulted in a reduction in variance, with a trade-off of a slight increase in the model's bias [78].

Appendix A.3. Extreme Gradient Boosting classifier (XGBClassifier)

EXtreme Gradient Boosting classifier (XGBClassifier) implements gradient boosted decision trees designed for speed and performance [79][80]. It is known for its efficiency at handling large datasets and its effectiveness in improving model performance through boosting. XGBoost also includes regularization to reduce overfitting.

Appendix A.4. Light Gradient Boosting Machine (LGBMClassifier)

Light Gradient Boosting Machine (LGBMClassifier) is a gradient boosting framework that utilizes tree-based learning algorithms. It is developed for distributed and efficient training, particularly on large datasets [81]. LGBM is known for its high efficiency, handling large data, and lower memory usage. Its efficiency comes from histogram-based optimizations in the tree learning process. LGBMClassifier utilizes tree-based learning algorithms because they offer a balance of accuracy, efficiency, and flexibility, making them highly suitable for structured data and large-scale classification problems. The combination of gradient boosting and optimized tree construction techniques further enhances its performance and scalability.

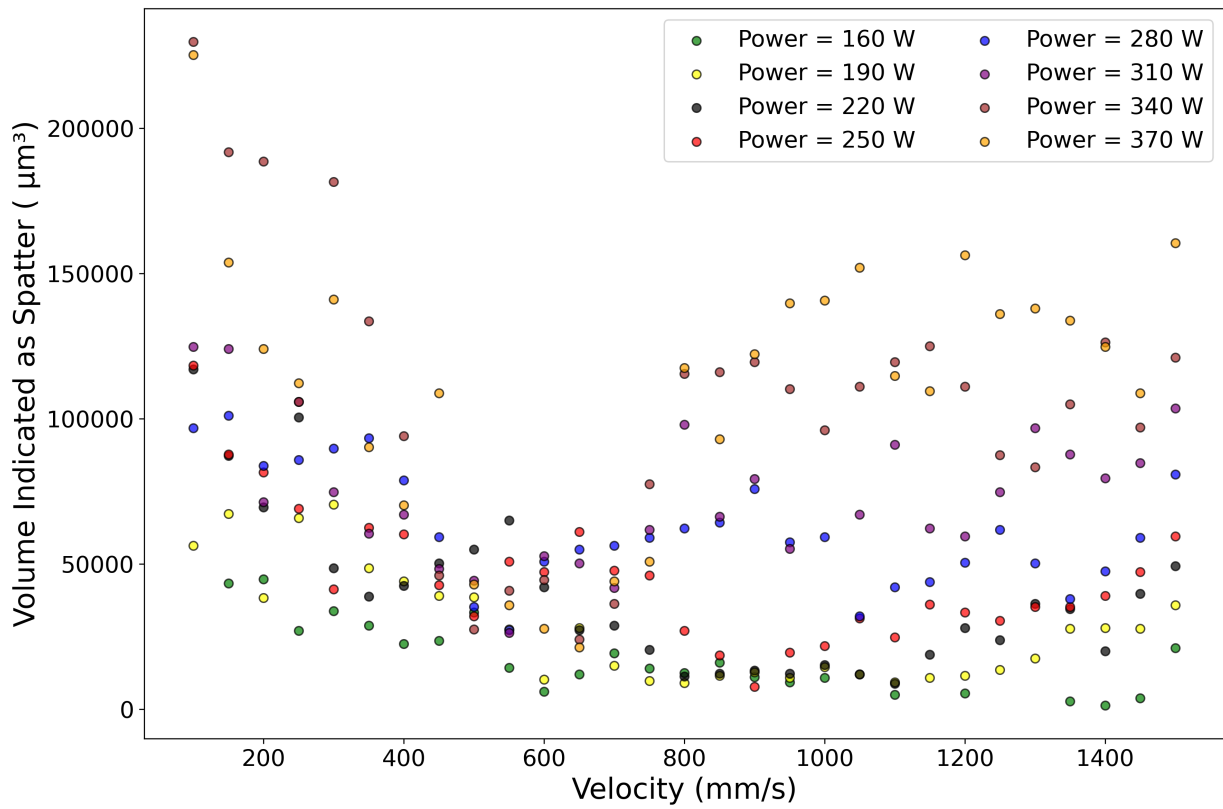


Figure A.16: Trend in power and velocity variation on the volume indicated as spatter.

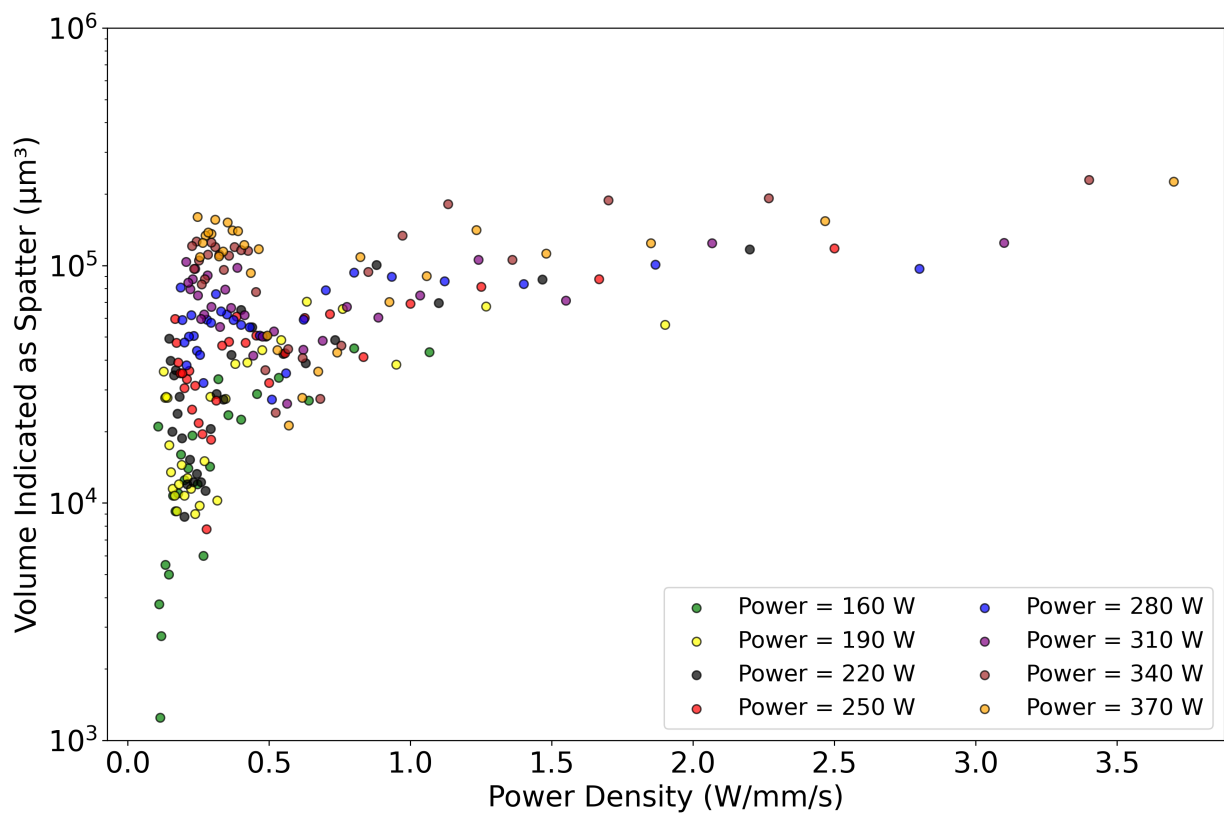


Figure A.17: Relationship between the energy density on the volume indicated as spatter.